Chapter 3

Mid-Infrared Spectroscopy of Submillimeter Galaxies: Extended Star Formation in Massive High-Redshift Galaxies

We have completed an observing program with *Spitzer* IRS to study the mid-IR properties and investigate the energetics of 24 SMGs [1]. This program comprises the largest sample of SMGs observed with *Spitzer* IRS and covers the full extent of properties of the radio-identified population of SMGs in the redshift range of $z \sim 0.65$–3.2. We observe broad PAH emission features in more than 80% of our sample. We find that the median mid-IR spectrum is well-described by a starburst component with an additional power law, $F_\nu \sim \nu^{-2}$, likely representing a $\lesssim 35\%$ AGN contribution to the bolometric luminosity. Our results thus confirm that even in the case of SMGs with a significant AGN contribution revealed at other wavelengths, starburst activity dominates the bolometric luminosity. We find that SMGs show weaker silicate absorption at ~ 9.7 μm than local ULIRGs. This implies that the continuum and PAH emitting regions of the SMGs are less obscured than in similarly luminous local ULIRGs. We interpret this as evidence for a more extended distribution of cool and warm dust in SMGs compared to the more compact starbursts in local ULIRGs. We also find stronger 6.2 μm PAH emission in SMGs (relative to the 7.7 μm PAH feature) than in local starbursts. These results suggest that SMGs are not simply high-redshift

[1] This chapter has been submitted to ApJ in similar form as Menéndez-Delmestre et al. 2008.

analogs of either local ULIRGs or nuclear starbursts, but instead they appear to have star formation which resembles that seen in less-extreme star-forming environments at $z \sim 0$ – suggesting their intense activity is distributed across a far larger region than the $\sim$ 1-kpc nuclear bursts in local ULIRGs.

3.1 Introduction

In Chapter 2 we presented the *Spitzer* IRS results for the first five SMGs observed in the program (Menéndez-Delmestre et al. 2007), which complemented earlier IRS results for two SMGs at $z \sim 2.8$ presented by Lutz et al. (2005). Since then, Valiante et al. (2007) and Pope et al. (2008) obtained IRS spectra of nine SMGs in blank field and cluster lens surveys and of 13 SMGs from the GOODS-North Field, respectively. Here we present our results for our full sample of 24 SMGs, comprising the largest sample of SMGs observed to date with *Spitzer* and nearly doubling the number of SMGs observed with IRS. We discuss our sample selection and observing strategy in §3.2. The steps comprising the reduction and analysis of the spectra are discussed in §3.2 and §3.3. Our results are presented in §3.4 and discussed in detail in §3.5. We assume a ΛCDM cosmology, with $H_0 = 71\,\mathrm{km\,s^{-1}\,Mpc^{-1}}$, $\Omega_M = 0.27$ and $\Omega_\Lambda = 0.73$.

3.2 Observations and Reduction

The SMGs in our program were selected from the sample of 73 spectroscopically-confirmed, radio-identified SMGs in C05. We aimed for full coverage of the range in redshifts, radio, submm and total IR luminosities present in the C05 sample (see Fig. 3.1) to build a sample representative of the radio-identified SMG population in general. We note that several of the SMGs from the C05 spectroscopic sample fall in the GOODS-North region and were included in the IRS studies focused on that field (Pope et al. 2008). Together with our sample, these are effectively part of a larger IRS study of the C05 survey which covers a total of 33 SMGs (or 45% of the parent C05 sample).

Table 3.1. Summary of *Spitzer* IRS Observations

Name	R.A.[a] ($h\,m\,s$)	Dec. ($^\circ\,'\,''$)	z^b_{opt}	Date	LL1 (ramp [s] × cycles)	LL2 (ramp [s] × cycles)
SMM J030227.73	03 02 27.73	+00 06 53.5	1.408	Jan. 2006	120 × 30	120 × 30
SMM J030231.81	03 02 31.81	+00 10 31.3	1.316	Feb. 2006	120 × 30	120 × 30
SMM J105151.69	10 51 51.69	+57 26 36.0	1.147	May 2006	120 × 30	120 × 30
SMM J105158.02	10 51 58.02	+57 18 00.3	2.239	May 2006	120 × 30	–
SMM J105200.22	10 52 00.22	+57 24 20.2	0.689	May 2006	120 × 30	120 × 30
SMM J105227.58	10 52 27.58	+57 25 12.4	2.142	May 2006	120 × 30	–
SMM J105238.19	10 52 38.19	+57 16 51.1	1.852	May 2006	120 × 30	120 × 30
SMM J105238.30	10 52 38.30	+57 24 35.8	3.036	May 2006	120 × 30	–
SMM J123549.44	12 35 49.44	+62 15 36.8	2.203	May 2006	120 × 30	–
SMM J123553.26	12 35 53.26	+62 13 37.7	2.098	May 2006	120 × 30	–
SMM J123707.21	12 37 07.21	+62 14 08.1	2.484	May 2006	120 × 30	–
SMM J123711.98	12 37 11.98	+62 13 25.7	1.992	May 2006	120 × 30	120 × 30
SMM J123721.87	12 37 21.87	+62 10 35.3	0.979	May 2006	120 × 30	120 × 30
SMM J163639.01	16 36 39.01	+40 56 35.9	1.495	Aug. 2005	120 × 30	120 × 30
SMM J163650.43	16 36 50.43	+40 57 34.5	2.378	Sept. 2005	120 × 30	–
SMM J163658.78	16 36 58.78	+40 57 28.1	1.190	Sept. 2005	120 × 30	120 × 30
SMM J221733.02	22 17 33.02	+00 09 06.0	0.926	June 2006	120 × 20	120 × 30
SMM J221733.12	22 17 33.12	+00 11 20.2	0.652	Nov. 2005	120 × 15	120 × 15
SMM J221733.91	22 17 33.91	+00 13 52.1	2.555	June 2006	120 × 30	–
SMM J221735.15	22 17 35.15	+00 15 37.2	3.098	June 2006	120 × 30	–
SMM J221735.84	22 17 35.84	+00 15 58.9	3.089	June 2006	120 × 30	–
SMM J221737.39	22 17 37.39	+00 10 25.1	2.614	June 2006	120 × 30	–
SMM J221804.42	22 18 04.42	+00 21 54.4	2.517	June 2006	120 × 30	–
SMM J221806.77	22 18 06.77	+00 12 45.7	3.623	June 2006	120 × 30	–

[a] Radio position from C05 compilation.

[b] Spectroscopic redshifts from C05.

While we aimed to span the full range in multi-wavelength properties of radio-identified SMGs, to have a realistic chance of detecting the galaxies with IRS we selected the 24 SMGs with the highest estimated 24 μm fluxes.[2] As 24 μm observations were not available at the time of the proposal, we estimated 24 μm fluxes for the SMGs in C05 from fitting the SEDs to the radio (1.4 GHz), submm (850 μm) and available optical photometric data points (see C05 and references therein). We note that selection of 24 μm-bright sources (albeit estimated) may introduce a two-sided selection effect. Selection based on bright 24 μm-fluxes will preferentially pick out the hot dust emission in AGNs. However, at redshifts $z \sim 2$, the 7.7 μm-PAH feature is redshifted onto the 24 μm band: this is a prominent emission feature, associated with star-formation activity and will result in a boosted 24 μm flux. We discuss this potential selection bias in more detail in §3.4.5. From a parallel mid-IR imaging survey of the radio-identified SMGs in C05 with the Multiband Imager for *Spitzer* (MIPS) by Hainline et al. (2009) our IRS subsample has MIPS 24 μm band fluxes in the range $S_{24\ \mu\mathrm{m}} \sim 0.09$–$0.85$ mJy with a median value of $< S_{24\ \mu\mathrm{m}} >= 0.33 \pm 0.18$ mJy.

The details of our observations are summarized in Table 3.1. We observed all our targets using the low-resolution ($R \sim 57$–126) Long-Low (LL) observing module of IRS. The slit width for this module is $\sim 10.7''$, which corresponds to roughly 100 kpc at $z \sim 2$, and so each target is fully enclosed in the observed slit and is thus treated as a point source. With shared coverage of the first LL order (LL1: 19.5–38.0 μm) and the second LL order (LL2: 14.0–21.3 μm) we aimed to cover rest-frame emission longwards of 6 μm to search for PAH emission and for any silicate absorption at 9.7 μm. With a redshift range of $z = 0.65$–3.2 for the full sample, the LL1 IRS module alone provides the relevant coverage for SMGs with $z \gtrsim 2.2$; while the LL2 module is also required for SMGs with $z \lesssim 2.2$. We observed each target at two different nod positions for a total integration time of 1–2 hours with each module. The data were obtained between August 2005 and June 2006.

[2]We used the online tool SPEC-PET to calculate estimated S/N for galaxies according to the estimated $S_{24\mu\mathrm{m}}$ value (http://ssc.spitzer.caltech.edu/tools/specpet/).

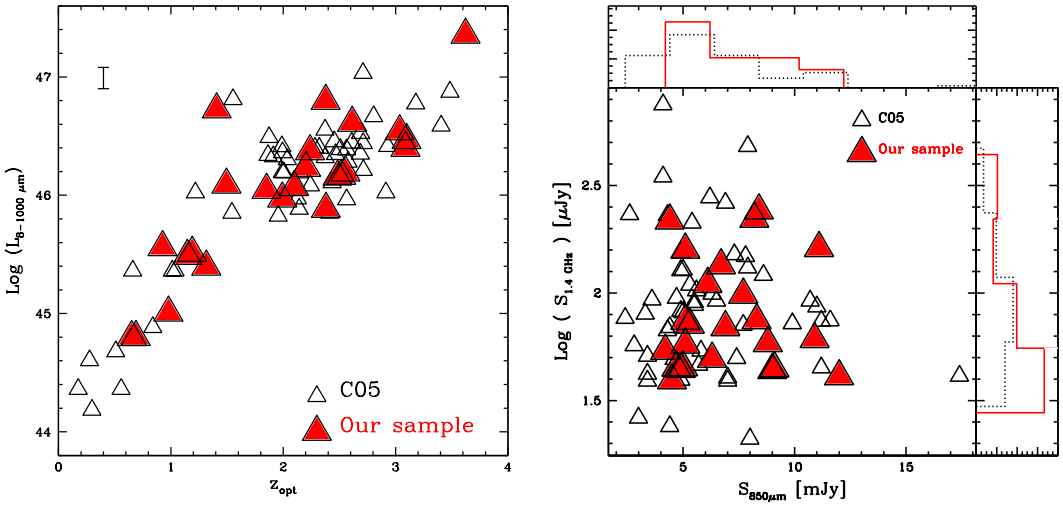

Figure 3.1 (**Left:**) The distribution of redshifts and IR luminosities (8–1000 μm) of the parent sample of radio-identified SMGs compiled by C05 with our IRS subsample highlighted. We plot a representative error on the IR luminosities. (**Right:**) The distribution of radio and submillimeter fluxes for the full C05 sample and those in the subsample observed with IRS. The histograms show the cumulative distribution of the full sample and the IRS subsample. These plots demonstrate that the IRS sample is representative of the parent sample of radio-identified SMGs, covering the full range in radio and submm properties, redshift and IR-luminosity.

We reduced the data using the *Spitzer* IRS S14 pipeline.[3] To ensure homogeneity throughout the sample, we reprocessed the raw data from our earlier results (Menéndez-Delmestre et al. 2007), which had been processed by the S13 pipeline. We performed additional cleaning of the 2D spectra using the *SSC* utility IRSCLEAN [4] to remove rogue pixels, by creating a mask for each Astronomical Observing Request (AOR). We use the rogue pixel mask associated with the observing cycle as a base and then identify additional deviant pixels in a *superdroop* file resulting from the averaging of all droop files within a single AOR. We relied on differencing between the two nod positions to subtract the residual background. To do this, we median-combined all cycles for science images with the same module order (LL1 or LL2) and nod position. For each module order, we then subtracted the median of all science images at one nod position from that of the other nod position.

For each LL order, we used the SPitzer IRS Custom Extraction [5] (SPICE) software to extract flux-calibrated 1D spectra from each 2D sky-subtracted median-combined nod. We used the *optimal extraction* mode recently included in SPICE. Optimal extraction entails taking a weighted average of profile-normalized flux at each wavelength to increase the S/N in IRS observations of faint sources (Horne 1986; Narron et al. 2006). Flux calibration is based on observations of a standard star during the same observing cycle as the science observations and has a 10% uncertainty (see IRS Data Handbook [6] for details). The SPICE-extracted 1D spectra for the different nods within one LL order were then median-combined. We combined the orders using IRAF to produce a final spectrum for each target, excluding the noisy edges at $\lambda_{obs} \lesssim 14.2$ μm and $\lambda_{obs} \gtrsim 35$ μm. The resulting spectra are shown in Fig. 3.2.

[3] http://ssc.spitzer.caltech.edu/irs/dh/
[4] http://ssc.spitzer.caltech.edu/archanaly/contributed/irsclean
[5] http://ssc.spitzer.caltech.edu/postbcd/spice.html
[6] http://ssc.spitzer.caltech.edu/irs/dh/

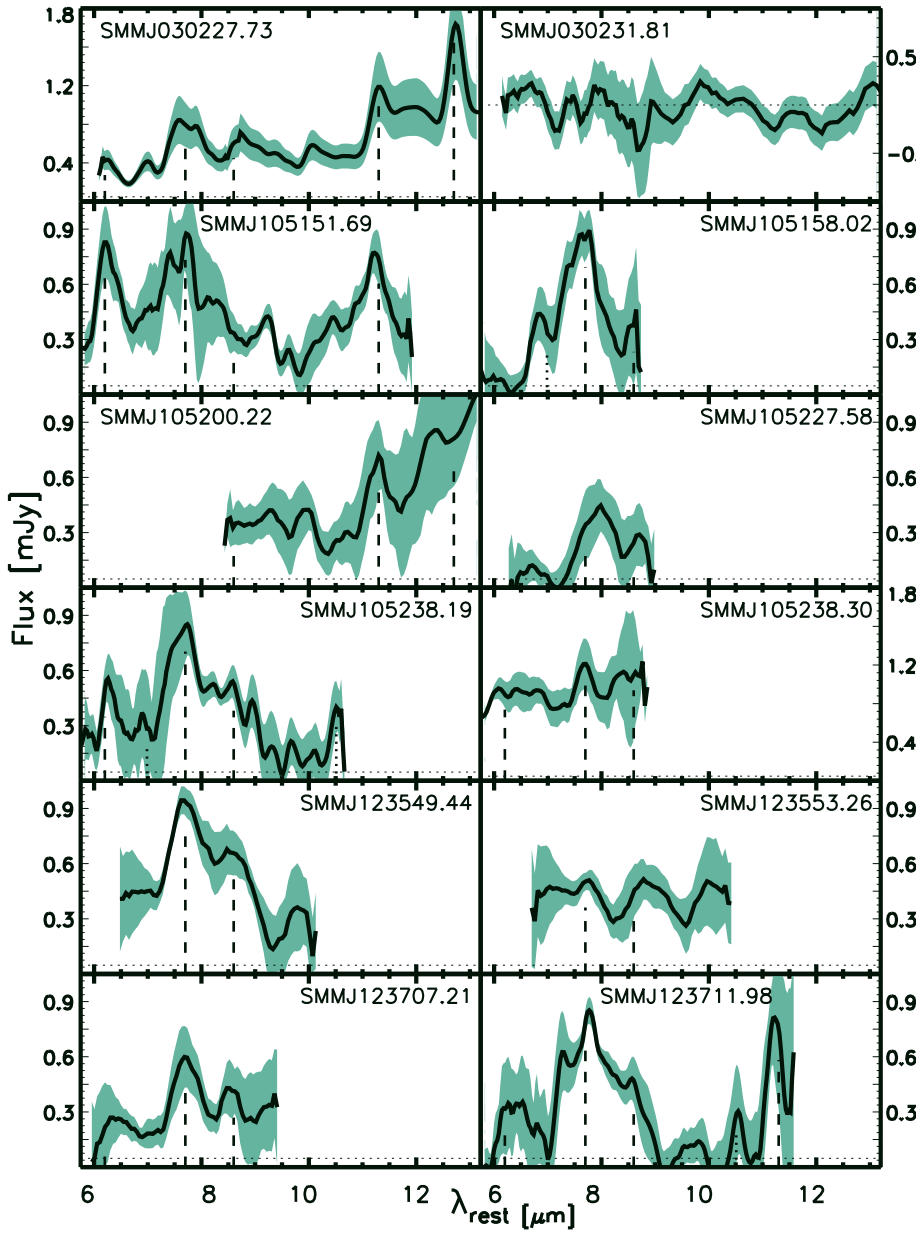

Figure 3.2 The rest-frame mid-IR spectra of all 24 SMGs in our sample, smoothed to the instrument resolution ($\Delta\lambda \sim 0.3$ μm at $\lambda \sim 24$ μm). The zero level for each spectrum is denoted by a horizontal short-dashed line and the shading represents the flux uncertainty, as given by SPICE. We do not detect SMM J030231.81. The locations of PAH features at 6.2, 7.7, 8.6, 11.3 and 12.7 μm are indicated by the dashed lines and these features are visible in a large fraction of our sample. The position of tentative narrow line emission from [ArII] (6.99 μm) and/or [SiV] (10.51 μm) are shown by dotted lines in SMM J105158.02, SMM J105238.19, SMM J123711.98, SMM J123721.87, SMM J163639.01, SMM J221733.91 and SMM J221735.15.

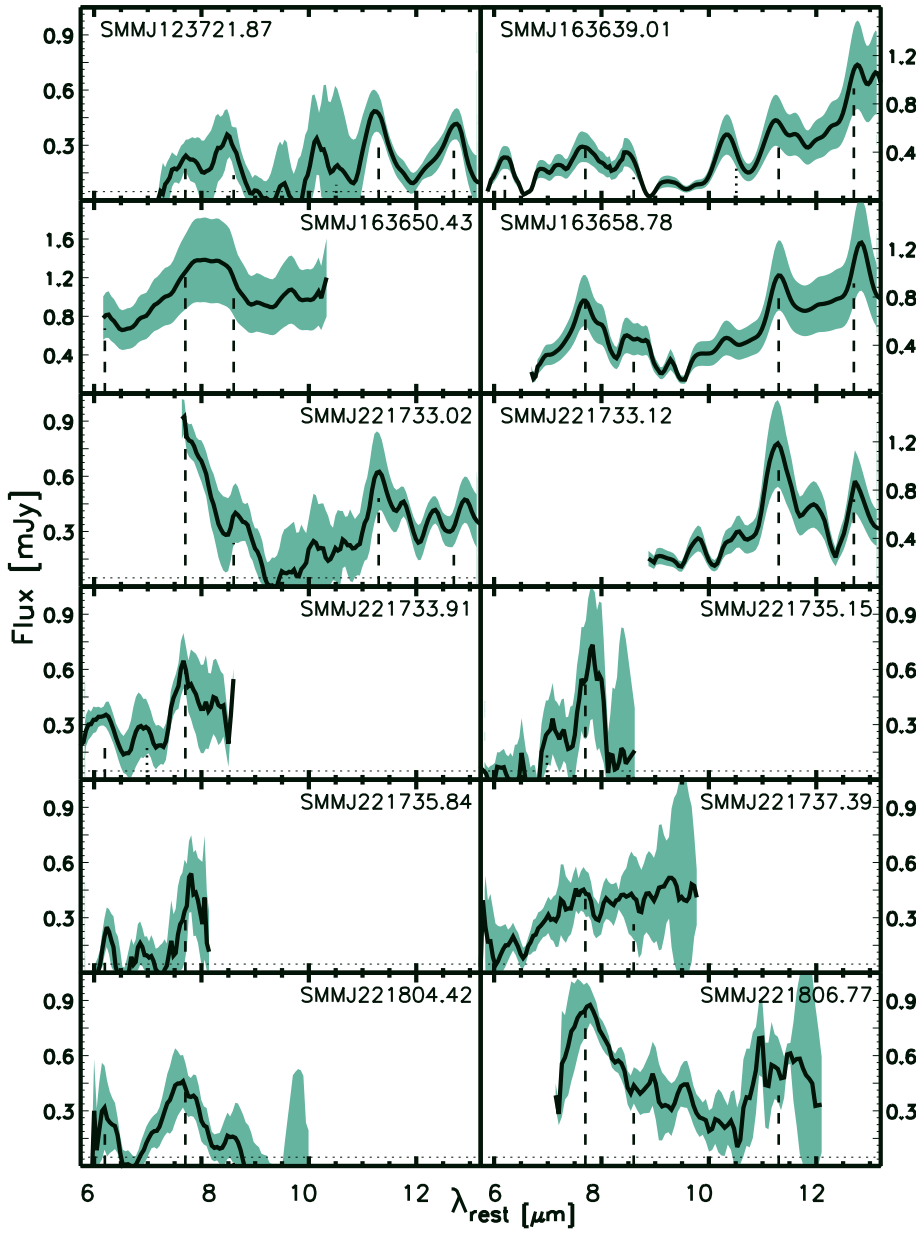

Fig. 3.2. — Continued.

3.3 Analysis

The spectra in Fig. 3.2 show a range of emission and absorption features. One of the key advantages of our survey over previous studies is the availability of spectroscopic redshifts for the entire sample from C05. With spectroscopic redshifts in hand, we have a priori knowledge of the observed wavelengths where emission and absorption features are expected. We therefore identified PAH features, silicate absorption centered at ~ 9.7 μm and a number of possible forbidden narrow emission lines, such as [ArII] (6.99 μm) and [SIV] (10.51 μm). We see that a large fraction of our sample show PAH emission and we mark these and the other spectral features on Fig. 3.2.

To derive quantitative estimates of the strength of the emission and absorption features and determine their precise wavelengths we need to fit the spectra. However, given our modest integration times (Table 3.1), we reach a signal to noise (S/N) of only 1–5 in the continuum emission at 24 μm [7]. At this S/N we found that intricate spectral fitting programs (e.g., PAHFIT; Smith et al. 2007) are not appropriate. We thus adopted a simple and straight-forward fitting approach which we describe below.

The measurements of the fluxes and EWs of features in the spectra required that we first determine the continuum level for each spectrum before measuring the strength of each individual emission and absorption feature. The resulting EW and flux measurements are extremely sensitive to the fitting method selected, particularly in the determination of the continuum level. A number of alternative fitting methods have been used by different authors, making a fair comparison of PAH strengths in different samples a rather subjective and delicate issue, as discussed by Sajina et al. (2007). In particular, the prevalence of interactive fitting methods has further complicated the reproducibility of mid-IR properties between samples. Hence in this work we have adopted a method of continuum and PAH fitting that ensures complete reproducibility. Moreover, in order to make fair comparisons between the SMGs in our sample and other low- and high-redshift sources, we have re-measured all the mid-IR features in all of these samples using our method. We have applied our method

[7] S/N was determined within a λ-window of $\Delta\lambda \sim 1.4$ μm on the individual nod-subtracted 2D spectra

to select local ULIRGs from the Bright *IRAS* sample studied by Armus et al. (2006, 2007) and Desai et al. (2007), the low-redshift nuclear starburst-dominated galaxies presented by Brandl et al. (2006) and the mid-IR selected high-redshift sources of Sajina et al. (2007). As we noted earlier, we have also included in our comparisons the 13 SMGs in the GOODS-North field studied by Pope et al. (2008), nine of which have optical redshifts measured by C05 and thus naturally complement our sample.

The thermal mid-IR continuum, arising either from starburst or AGN activity can be described by a power-law, $S_\nu \sim \nu^{-\alpha_{\rm MIR}}$, where the value of the power-law index $\alpha_{\rm MIR}$ gives an indication of the steepness of the spectrum. Flatter mid-IR continua with low power-law indices ($\alpha_{\rm MIR} \lesssim 0.5$) are usually associated with unobscured AGNs, where emission from the hot dust close to the AGN is readily observed. Steeper continua ($\alpha_{\rm MIR} \gtrsim 0.5$) are on the other hand associated with starburst activity, but can also be found in dust-obscured AGNs. Hence we determined the power-law continuum index $\alpha_{\rm MIR}$ for the spectra in our sample to: (1) characterize the continuum slope and investigate the underlying energetics, and (2) to define the continuum level on which PAH emission features are superimposed.

To determine $\alpha_{\rm MIR}$ we use the χ^2 minimization IDL routine LINFIT to obtain the best linear fit to each SMG spectrum in $\log(S_\nu)$–$\log(\nu)$ space (see Fig. 3.3). We first obtain the best linear fit to each full spectrum and calculate the rms in the (original − fit) residual spectrum. Then, we identify those wavelength regions in the original spectrum where the data points lie more than 1× the rms away from this first linear fit. In this way, we automatically identify the wavelength regions where emission and absorption features are present. We then perform a second round of linear fitting, where we exclude these regions from the fit. We adopt the results of this second fit as our final continuum, with the influence of emission and absorption features minimized. The uncertainty in the continuum level is established considering the flux uncertainty given by SPICE for each individual spectrum. These flux uncertainties propagate into an uncertainty of $\sim 20\%$.

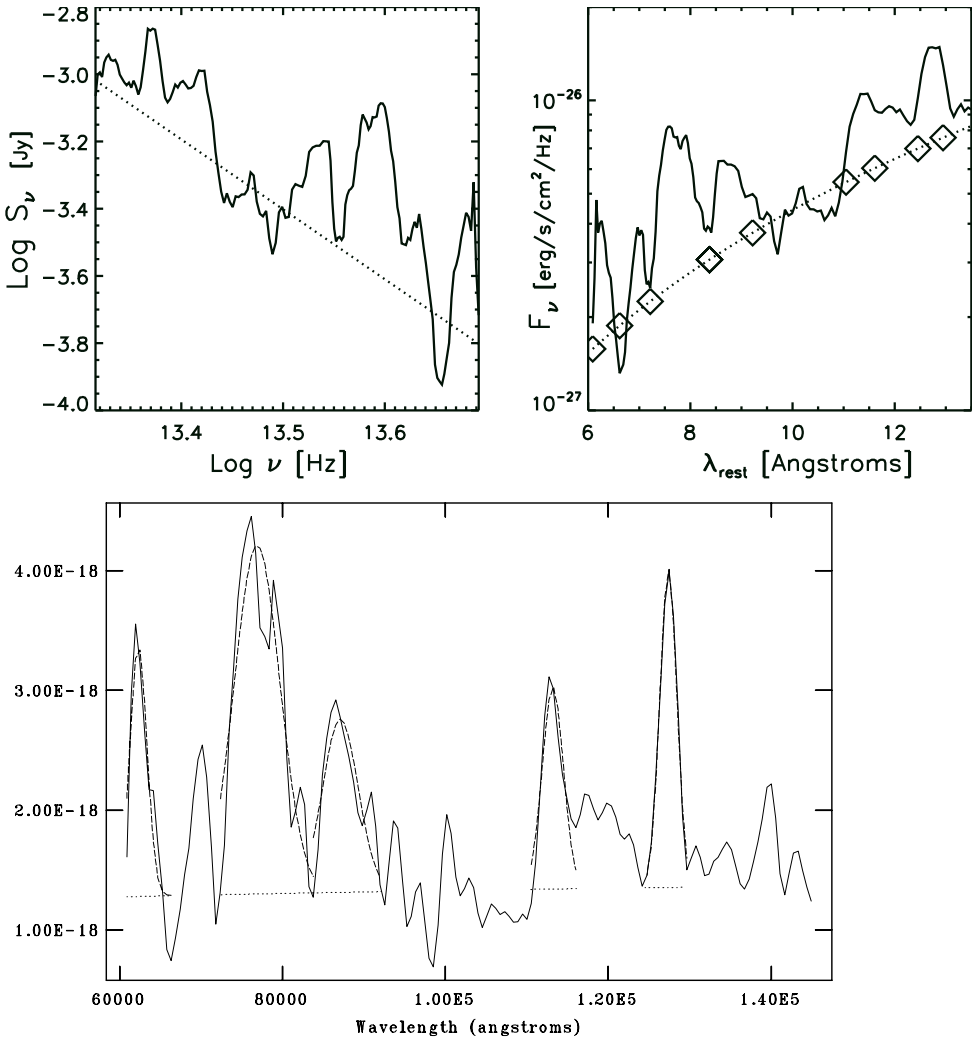

Figure 3.3 (**Top Left:**) Sample spectrum in $Log[S_\nu] - Log[\nu]$ space that illustrates our approach to continuum determination. The solid line is the spectrum of SMM J030227.73 and the dotted line is the best fit continuum determined through the method described in §3.3. (**Top Right:**) For each PAH feature, we defined a fitting window covering a narrow wavelength range centered at the expected central PAH wavelengths ($6.22, 7.598, 8.61, 11.33, 12.62$ μm; Draine & Li 2007). The edges of these fitting windows are denoted in this figure by open diamonds on the spectrum. (**Bottom:**) Mid-IR spectrum of SMM J030227.73 with flux expressed in units of λS_λ. The gaussian fit for each PAH feature is shown as dashed curves.

Having determined the continuum, we search for the presence of PAH emission features at 6.2, 7.7, 8.6, 11.3 and 12.7 μm. Since our targets have a range in redshift, $z \sim 0.65$–3.2, the wavelength coverage varies from 6–22 μm for the lowest redshift SMGs to 4.2–8.3 μm for the highest redshift. Out of all detected SMGs in our sample, 90% include coverage of the 7.7 μm region of the spectrum, thus providing a large sample of 20 SMGs to investigate the spectral features within this important wavelength region. We define a wavelength window around each spectral feature and use the IRAF task SPLOT to fit the PAH features with individual gaussians, where the center and FWHM are left as free parameters within the fitting window. We create a cursor file specifying the fitting windows and continuum level for each spectrum to automate the fitting process and thus avoid the lack of reproducibility inherent to other interactive fitting tasks. The wavelength regions used to fit the 6.2, 7.7, 8.6, 11.3 and 12.7 μm PAH features were approximately 6.026–6.617, 7.031–8.302, 8.242–8.922, 10.813–11.812, 12.409–13.029 μm, respectively (see Fig. 3.3). We adopt the SPLOT output uncertainties in the resulting EWs and luminosities, which account for the noise level present in the spectra. These errors are indicated in Table 3.2 and correspond to an average uncertainty of $\sim 30\%$. We derive a redshift associated with each PAH feature from its observed central wavelength. The final PAH-based redshift for spectra displaying multiple PAH features corresponds to the weighted mean of the redshifts derived from the individual PAH features, where the weights are provided by the PAH fitting uncertainties.

Finally, to determine the depth of the silicate absorption, we define the optical depth as $\tau_{9.7\ \mu\mathrm{m}} = \log_{10}[S_{cont}/S_{obs}]$, where S_{obs} is the flux level observed at 9.7 μm and S_{cont}, the interpolated flux of continuum in the absence of any absorption. We measure the latter from our power law continuum fit. The EWs and fluxes for PAH emission and absorption features we derive are listed in Table 3.2.

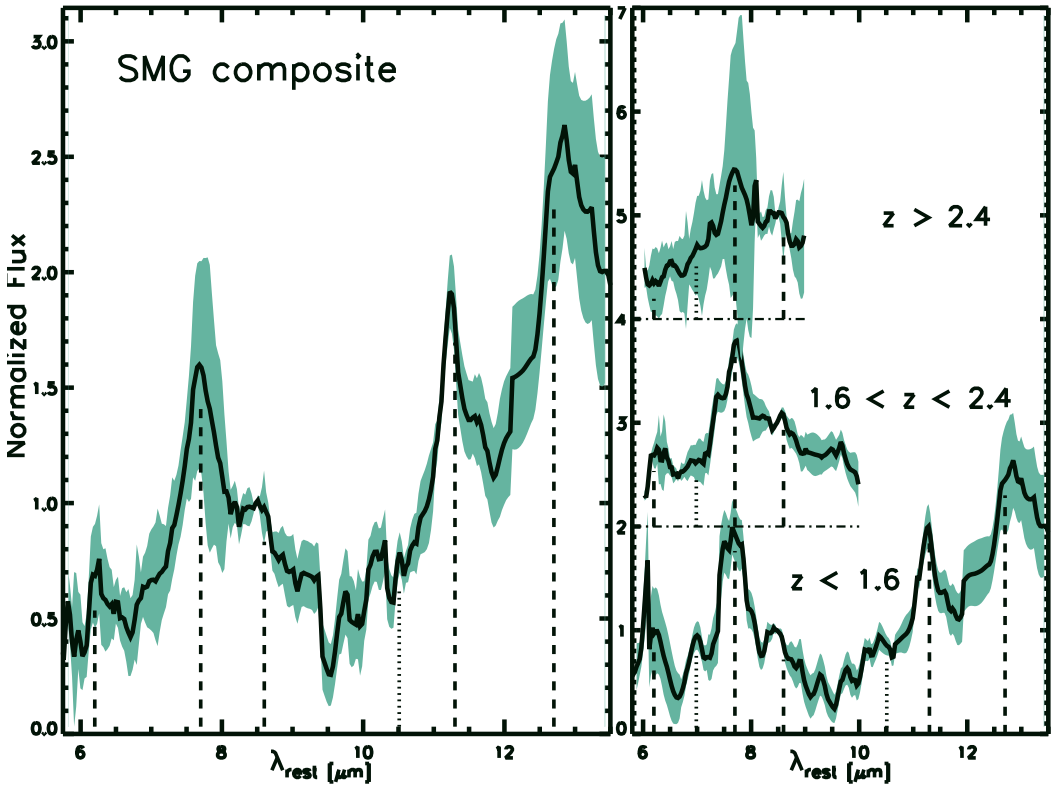

Figure 3.4 (**Left:**) The median-combined rest-frame composite spectrum of 22 SMGs detected in our sample, with the shaded area representing the 1-σ sample standard deviation. We assume optical redshifts (C05), except for the five SMGs in which PAH features suggest an alternate redshift (see Table 3.2). The composite spectrum is dominated by strong PAH emission at 6.2, 7.7, 8.6, 11.3 and 12.7 μm, with an underlying red continuum. All the spectra are normalized by their flux at $\lambda = 8.5\,\mu$m in the rest-frame (see §3.3.1 for details). (**Right:**) Composite spectra for subsets of SMGs in three separate redshift bins, where the zero level of each spectrum is denoted by a dash-dotted horizontal line. These demonstrate that at $\lambda > 10$ μm our composite spectrum is dominated by sources at $z < 1.6$.

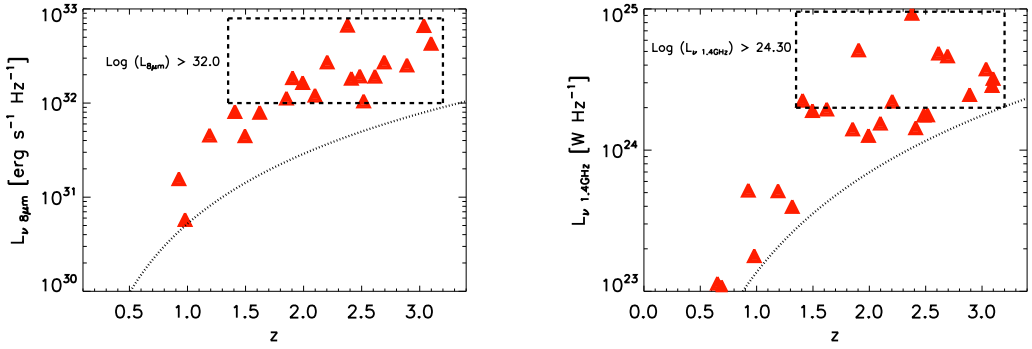

Figure 3.5 (**Left:**) Rest-frame 8 μm luminosity, measured from rest-frame IRS spectra, as a function of redshift for the SMGs in our sample. The dotted curve represents the lowest 8 μm luminosity accessible to *Spitzer* IRS at each redshift, assuming a flux sensitivity of $S_{24\ \mu\mathrm{m}} \sim 0.2\,\mathrm{mJy}$. The dashed box denotes the luminosity-complete subsample of SMGs with $\mathrm{L}_{8\ \mu\mathrm{m}} \gtrsim 10^{32}$ erg s^{-1} from which we build composite spectra based on 24 μm-brightness. (**Right:**) Similar plot for the rest-frame radio luminosity density at 1.4 GHz for the SMGs in our sample. The dotted line represents the 3-σ flux sensitivity ($\sim$ 30 μJy) of the radio observations discussed in C05. The dashed box encloses the SMGs with $\mathrm{L}_{1.4GHz} \gtrsim 2 \times 10^{24}$ erg s^{-1} Hz^{-1} that comprise the radio-luminosity-complete sample used to create SMG composites based on radio-brightness. See §3.3.1 for details.

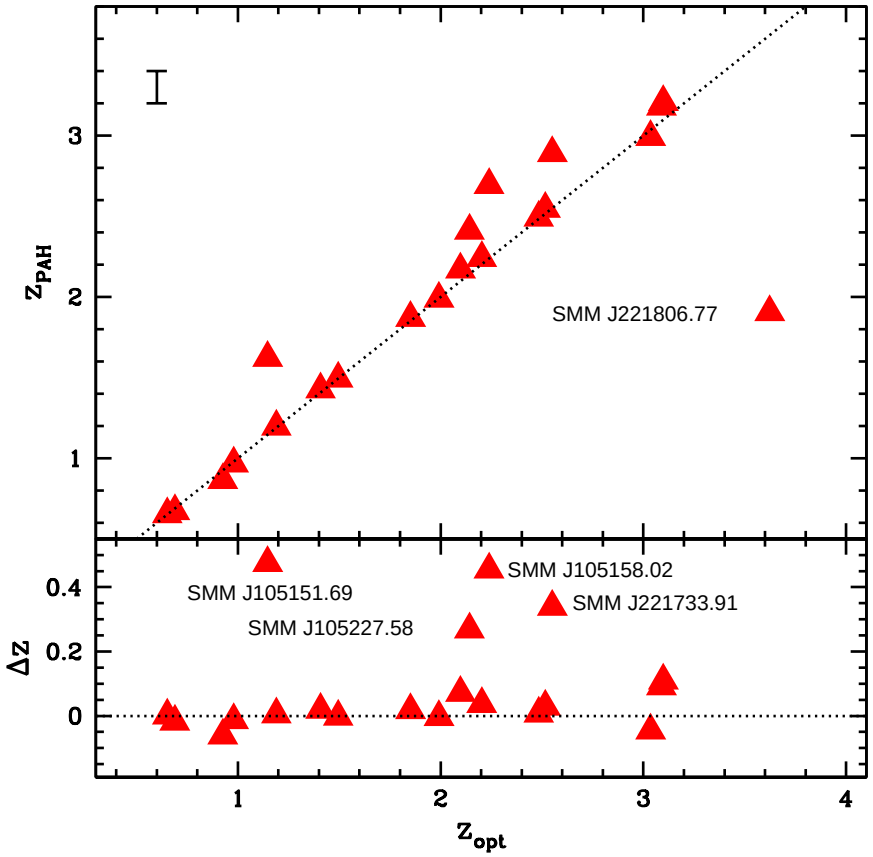

Figure 3.6 A comparison of the PAH-derived redshifts with the rest-frame UV redshifts for the SMGs in our sample (C05). Five out of the 23 detected SMGs have multiple PAH features that suggest a redshift significantly different from the optical one, namely SMM J105151.69, SMM J105227.58, SMM J105158.02, SMM J221733.91 and SMM J221806.77. Four out of these five SMGs have mid-IR spectra displaying one particularly prominent feature that we associate with the 7.7 μm PAH line. The presence of additional fainter features confirm the validity of this assumption. The typical uncertainty in the PAH-based redshifts is shown by the error bar in the top panel.

3.3.1 Composite Spectra

In the interest of obtaining a representative spectrum for the sample as a whole, with a higher S/N to enable identification of fainter underlying features, we also median-combined the individual spectra of the SMGs into a composite. The full collection of individual spectra in our sample cover the rest-frame wavelength range $\lambda \sim$ 5–22 μm. To reduce bias towards the mid-IR properties of SMGs within a narrower redshift range, we only include in the composite spectrum wavelengths covered by the data for *at least* five SMGs. The individual spectra in Fig. 3.2 also display a significant spread in rest-frame continuum level with $S_{9\mu\mathrm{m}} \sim 0.2$–$1.2\,\mathrm{mJy}$ and so we normalize them by their flux at a rest-frame wavelength of 8.5 μm. Only the spectrum of SMM J221733.12 does not cover this wavelength and is thus excluded from the composite. The final composite spectrum includes 22 detected SMGs, and is shown in Fig. 3.4. The sample standard deviation of the SMG composite spectrum increases towards longer wavelengths, in part reflecting the fact that fewer individual spectra contribute at $\lambda_{rest} \gtrsim 10$ μm. To better demonstrate the redshift ranges which contribute to the different wavelength regions in the composite (and their variations) we divide our sample into three different redshift bins and construct composite spectra of low-, intermediate- and high-redshift SMGs (see Fig. 3.4). We discuss these in §3.4.6.

We also take advantage of the range in properties covered by our sample (see Fig. 3.1) to investigate mid-IR spectral properties of different SMG sub-populations. We follow the method described above to construct composite spectra of subsamples of SMGs based on 24 μm and radio brightness to search for trends within our sample. However, composite spectra based on apparent brightness mix sources with different intrinsic luminosities at different redshifts: we attempt to minimize this bias in these composites by defining luminosity-complete sub-samples of SMGs. First, we restrict the sample of SMGs that go into each composite to those that fall within a redshift range for which we are close to complete in terms of mid-IR and radio luminosity. At the median redshift of our sample, $< z > \sim 2$, the observed 24 μm flux corresponds

to redshifted rest-frame 8 μm emission. Therefore, we define luminosity-complete sub-samples of SMGs by using the rest-frame luminosities at 8 μm and at 1.4 GHz.[8] We impose a luminosity cut and select all SMGs with luminosities greater than the limiting luminosity (see Fig. 3.5). To build the 24 μm-composites we restrict the parent sample to SMGs with $L_{8\ \mu m} \gtrsim 10^{32}$ erg s^{-1}. For the radio composite, we include SMGs with $L_{1.4GHz} \gtrsim 2 \times 10^{24}$ erg s^{-1} Hz^{-1}. As a result, low-redshift SMGs with the lowest mid-IR and radio luminosities within the sample, even though they have the highest apparent fluxes, are excluded from the 24 μm- and radio-brightness composites. We discuss these composites in §3.4.5.

3.4 Results

Out of the 24 SMGs in our sample shown in Fig. 3.2, we detect PAH emission and continuum in 16 SMGs, PAH emission and no continuum in three SMGs, continuum but no PAH emission in another four SMGs and neither continuum nor PAH emission in only a single SMG (SMM J030231.81). Hence, our sample contains 19 SMGs with PAH emission and 20 with detectable continuum emission. In addition, marginal detections of [ArII] (6.99 μm) and [SiV] (10.51 μm) narrow-line emission were found in several individual SMGs (see Fig. 3.2). We give the emission and absorption line properties for the individual SMGs in Table 3.2. Results for the various composite spectra are presented in Table 3.3.

[8] $L_{1.4GHz} = 4\pi D_L^2 S_{1.4GHz}(1+z)^{-(\alpha+1)}$ W Hz^{-1}, assuming $\alpha = -0.8$, the average spectral index for star-forming galaxies (e.g., Yun et al. 2001)

3.4.1 PAH-based Redshifts

We have rest-frame UV redshifts for all the SMGs in our sample from optical spectroscopy (C05) using the blue-sensitive Low-Resolution Imaging Spectrograph (Oke et al. 1995; McCarthy et al. 1998) on Keck II. These spectroscopic redshifts allowed us to identify confidently faint emission and absorption features in the mid-IR spectra of individual SMGs. Nevertheless, with 19 SMGs displaying prominent PAH emission, we can determine a mid-IR redshift for each SMG based on the location of the redshifted PAH features and compare these to the rest-frame UV redshifts for these galaxies. PAH-based redshifts (z_{PAH}) for our sample are shown in Table 3.2 and are compared to the redshifts from C05 (z_{opt}) in Fig. 3.6. We note that PAH-derived redshifts have a large uncertainty ($\Delta z \sim 0.1$) arising from the intrinsically large width of PAH features ($\mathrm{FWHM}_{7.7\mu\mathrm{m}} \gtrsim 10^4\,\mathrm{km\,s^{-1}}$). Redshifts based on rest-frame UV features are thus more precise, although equally we note that as the optical emission in these systems does not trace the bolometric emission well, there are opportunities for them to be erroneous if the optical spectroscopic IDs are spatially offset from the true radio counterpart. The comparison in Fig. 3.6 demonstrates that the IRS spectra of the majority of the SMGs have features consistent with the rest-frame UV redshifts. However, there are five SMGs where the features suggest an alternate redshift (see Table 3.2) that is significantly different from the rest-frame UV redshift.

For the five SMGs with discrepant redshifts (see Fig. 3.7), the reasons for the disagreement are in all cases due to ambiguous line identifications resulting from low S/N features in the UV spectra, and so we discuss these individually. We note that these corrections to the redshifts have not significantly changed the interpretation of these sources.[9] We also note that one of the new PAH redshifts, for SMM J105158.02, strengthens the significance of the $z \sim 2.7$ SMG cluster/association discovered in Blain et al. (2004).

In the case of SMM J221733.91, an initial indication of a redshift around $z \sim 2.5$ from absorption features in a low S/N spectrum was apparently verified by a weak Hα

[9]Changes in redshift at the 10–20% level at $z \sim 2$ do not result in changes to the luminosities or temperatures beyond the associated calibration errors.

Table 3.2. Characterization of Mid-IR Spectral Features in Individual SMGs

SMM J	z_{opt}[a]	z_{PAH}[b]	$S_{6.2}$[c]	$EW_{6.2}$[d]	$S_{7.7}$	$EW_{7.7}$	$S_{8.6}$	$EW_{8.6}$	$S_{11.3}$	$EW_{11.3}$	$S_{12.7}$	$EW_{12.7}$	$\tau_{9.7}$[e]	$S_{24.0}$[f]
030227.73	1.408	1.43	5.51±0.97	0.18±0.03	20.44±1.50	0.65±0.05	7.92±1.40	0.25±0.04	5.47±1.00	0.17±0.03	6.93±0.84	0.21±0.03	>0.05	0.45
030231.81[g]	1.316	–	–	–	–	–	–	–	–	–	–	–	–	–
105151.69	1.147	1.62	16.07±1.20	0.50±0.04	17.60±2.50	0.79±0.09	–	–	4.40±1.60	0.43±0.15	–	–	>0.34	0.28
105158.02	2.239	2.69	–	–	8.56±7.10	–	0.69±7.50	0.83±0.06	–	–	–	–	–	0.12
105200.22	0.689	0.67	–	–	–	–	–	–	3.55±1.10	0.28±0.09	–	–	>0.49	0.88
105227.58	2.142	2.41	–	–	8.62±1.50	0.57±0.10	1.58±0.92	0.10±0.06	–	–	–	–	–	0.19
105238.19	1.852	1.87	9.13±0.64	0.33±0.02	26.11±1.10	1.39±0.06	6.45±1.20	0.43±0.08	–	–	–	–	>0.27	0.51
105238.30	3.036	2.99	–	–	6.05±0.62	0.04±0.00	–	–	–	–	–	–	–	0.75
123549.44	2.203	2.24	–	–	15.38±1.40	0.21±0.02	2.13±0.84	0.03±0.01	–	–	–	–	–	0.63
123553.26	2.098	2.17	–	–	4.18±1.30	0.09±0.03	5.19±1.70	0.16±0.05	–	–	–	–	–	0.39
123707.21	2.484	2.49	4.91±1.20	0.19±0.05	12.30±1.20	0.45±0.04	2.90±0.71	0.10±0.02	–	–	–	–	–	0.18
123711.98	1.992	1.99	8.75±0.96	0.41±0.04	36.07±1.70	2.47±0.12	6.68±1.30	0.58±0.11	5.55±0.67	0.85±0.10	–	–	>0.26	0.56
123721.87	0.979	0.97	–	–	2.77±1.10	0.72±0.30	4.35±1.00	1.32±0.31	4.29±1.00	1.16±0.28	2.77±1.20	0.93±0.41	>1.01	0.21
163639.01	1.495	1.49	8.32±1.00	0.51±0.06	10.00±1.80	0.64±0.11	4.45±1.30	0.25±0.08	3.75±1.50	0.20±0.08	6.31±1.50	0.33±0.08	>0.66	0.21
163650.43[h]	2.378	–	–	–	34.93±1.80	0.23±0.01	–	–	–	–	–	–	–	0.95
163658.78	1.190	1.20	–	–	20.51±1.70	0.89±0.07	4.72±1.40	0.20±0.06	5.46±1.10	0.23±0.05	4.95±1.10	0.20±0.05	>0.21	0.56
221733.02	0.926	0.87	–	–	–	–	3.05±1.10	0.21±0.08	4.97±1.10	0.70±0.15	–	–	>0.11	0.31
221733.12	0.652	0.65	–	–	–	–	–	–	13.89±1.60	1.53±0.17	4.77±1.30	0.57±0.16	>1.20	0.36
221733.91	2.555	2.89	5.33±1.20	0.16±0.04	9.45±1.20	0.36±0.05	–	–	–	–	–	–	–	0.24
221735.15	3.098	3.21	–	–	11.54±0.99	0.44±0.04	–	–	–	–	–	–	–	0.04
221735.84	3.089	3.18	3.98±0.61	–	6.28±0.61	–	–	–	–	–	–	–	–	0.01
221737.39[h]	2.614	–	–	–	–	–	–	–	–	–	–	–	–	0.14
221804.42	2.517	2.55	2.72±0.84	0.09±0.03	13.97±2.10	1.28±0.19	–	0.14±0.18	–	–	–	–	–	0.10
221806.77	3.623	1.91	–	–	25.98±0.97	0.17±0.01	4.90±0.67	0.04±0.01	7.35±0.67	0.12±0.01	–	–	–	0.60

[a] Optical redshifts from C05

[b] PAH-based Redshifts; see §3.4.1 for details.

[c] PAH fluxes in units of $10^{-15}\,\mathrm{erg\,s^{-1}cm^{-2}}$. Quoted errors correspond to PAH fitting uncertainties. An additional $\sim 20\%$ is attributed to flux calibration and continuum determination.

[d] PAH rest-frame EWs are expressed in units of μm

[e] Optical depth derived from Silicate-absorption feature. See §3.4.4 for details.

[f] Fluxes reported are average fluxes within $\lambda_{obs} = 23.7 \pm 2.35\mu$m in the individual IRS spectra, to reproduce the 24μm-MIPS band wavelength coverage.

[g] This SMG remained undetected.

[h] We do not report PAH measurements for SMGs with featureless spectra within the relevant PAH region or when PAH features are markedly blended, since relative fitting uncertainties become unduly dominant.

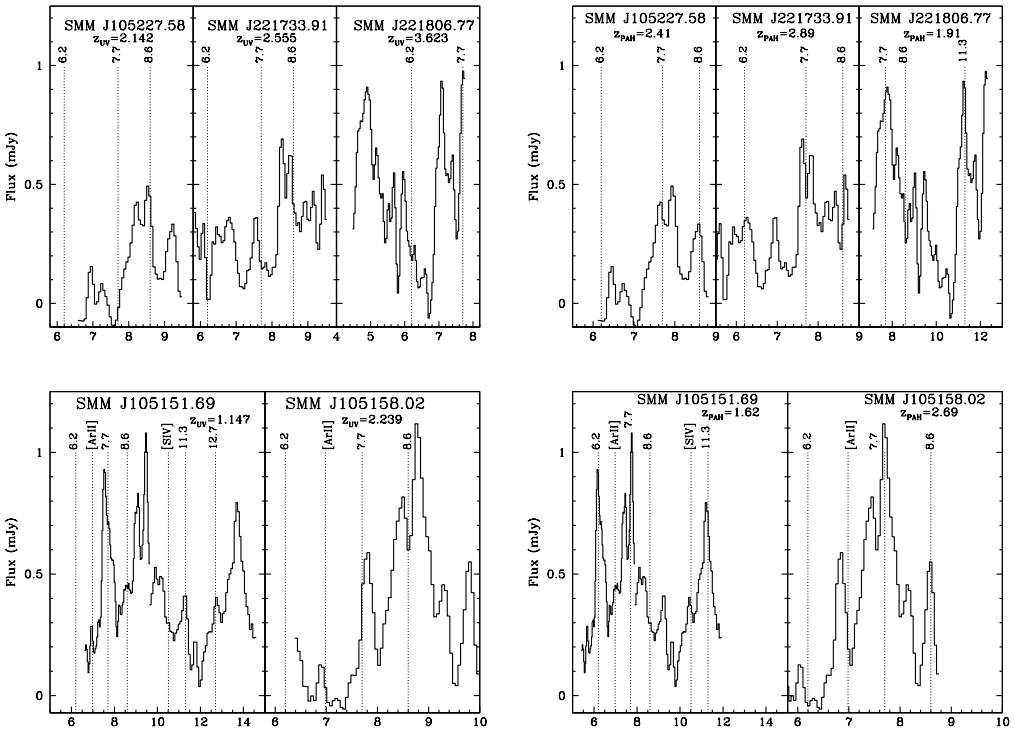

Figure 3.7 Alternate PAH-based redshifts for five individual SMG cases. (**Left:**) Rest-frame mid-IR spectra of SMM J105227.58, SMM J221733.91, SMM J221806.77, SMM J105151.69 and SMM J105158.02 assuming rest-frame UV redshifts (C05). (**Right:**) Rest-frame mid-IR spectra for the same five SMGs with the PAH-based redshifts. For clarity, we have excluded flux uncertainties, which are presented in Fig. 3.2. See §3.4.1 for details.

line at $z = 2.555$ (Swinbank et al. 2004). However, a deeper UV-spectrum, doubling the S/N, revealed an unambiguous $z = 2.865$ from multiple absorption features, consistent with the $z = 2.89$ found from the IRS spectrum.

Similarly with SMM J105227.58, the original noisy UV absorption line spectrum suggested $z = 2.142$. Subsequent deeper spectroscopy revealed this source to be $z = 2.407$ from weak Lyα emission, as well as CIV$_{1549}$ absorption and emission, consistent with the PAH redshift.

SMM J221806.77 was identified at $z = 3.623$ from a single weak emission line in a relatively sky-free spectral region and corroborated by a red continuum dropping out in the B band. The PAH-based redshift $z = 1.91$ suggests that the continuum of this source is more heavily reddened, and that the rest-frame UV emission feature is either noise or a superposed line detection from a different galaxy.

SMM J105158.02 was identified at $z \sim 2.2$ in the UV through various low S/N absorption features. An apparent Hα detection consistent with $z = 2.239$ was proposed as the true redshift (Swinbank et al. 2004), although a failed attempt to detect CO gas cast some doubt on the reality of the redshift (Smail et al., in prep). Re-analysis of a deeper UV spectra reveals a suite of absorption features consistent with $z = 2.694$ (SiII$_{1260}$, CII$_{1335}$).

Finally, for SMM J105151.69, an apparent emission line proposed as [OII]$_{3727}$ corresponding to $z = 1.147$ is not confirmed in later Keck spectra taken on this galaxy at a different position angle, and it has now been identified as an emission line galaxy slightly offset from the radio position. The PAH-based redshift of $z = 1.62$ is consistent with UV-spectra [CIII]$_{1909}$ absorption features and MgII$_{2800}$ emission features.

3.4.2 PAH Luminosities and PAH Ratios

The 7.7 μm PAH feature is the most prominent in the mid-IR spectra of star-forming galaxies and is particularly useful in studying star formation in sources at high redshift. We derive PAH luminosities from the integrated line fluxes presented in Table 3.2 and we plot these in Fig. 3.8. We find 7.7 μm PAH luminosities for SMGs

in the range $\sim 10^{43}$–$10^{45}\,\mathrm{erg\,s^{-1}}$ and hence that, as expected from their far-IR luminosities, SMGs have PAH luminosities that exceed those of local nuclear starbursts (Brandl et al. 2006) and ULIRGs [10] (Armus et al. 2007) by up to nearly four and two orders of magnitude, respectively. These PAH luminosities indicate that $\sim$ 1–5% of the bolometric luminosity in SMGs escapes in the form of PAH emission. We discuss the comparison of SMGs and local sources further in §3.4.6.1.

Different PAH emission features arise from distinct bending/vibrational modes of the PAH molecules (Draine & Li 2007). The different modes can be enhanced relative to each other as a result of varying PAH ionization state and PAH molecule size. Exposure to a more energetic radiation field may strip PAH molecules of peripheral H-atoms. A decrease in the fraction of neutral PAHs would diminish the strength of the 8.6, 11.3 and 12.7 μm PAH features, which are produced by the in-plane (8.6 μm) and out-of-plane (11.3, 12.7 μm) C-H bending mode. As a result, the 6.2 and 7.7 μm PAH features, which are thought to be produced by C-C skeleton vibration (Draine & Li 2007), would dominate. Within this context, the relative strength of PAH features can be used to probe the energetics of the underlying radiation field (e.g., Galliano et al. 2008). The size distribution of PAH molecules may also affect the observed relative strength of features: smaller PAHs ($N_C \lesssim 10^3$) tend to emit more strongly at 6.2 and 7.7 μm (Allamandola et al. 1989). In the hottest regions close to an AGN, sublimation of these smaller PAH molecules may result in a suppression of short-wavelength PAH emission features. Dust extinction has also been shown to play an important role in explaining the variation in the relative strength of PAH features. In particular, strong extinction can increase the 7.7/6.2 and 7.7/8.6 PAH ratios (Rigopoulou et al. 1999) due to an ice absorption feature at $\sim 6\,\mu$m (which reduces the 6.2 μm PAH emission, Spoon et al. 2002) and broad silicate absorption at $\sim 9.7\,\mu$m which reduces the strength of 8.6 μm PAH emission in highly extincted sources.

We derive the ratios of the integrated flux in the 6.2, 7.7 and 11.3 μm PAH features in our sample to investigate the energetics and extinction in the star-forming

[10] We include NGC 6240, Mrk 1014, UGC 5101, Arp 220, FSC 05189−2524, FSC 12112−0305, Mrk 273, FSC 14348−1447, FSC 22491−1808 from Armus et al. (2007).

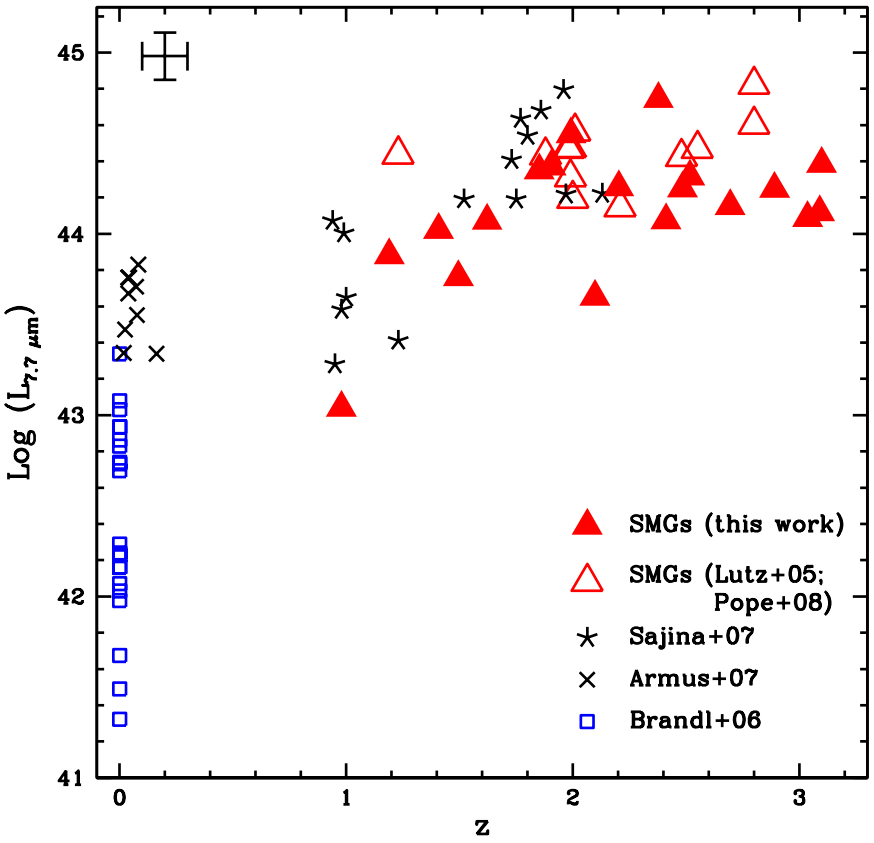

Figure 3.8 The 7.7 μm-PAH luminosities as a function of redshift for the SMGs in our sample. In addition we plot the two SMGs at $z \sim 2.8$ from Lutz et al. (2005) and the SMGs from Pope et al. (2008), many of which come from C05. For comparison we also plot aperture-corrected low-redshift nuclear starburst-dominated galaxies (Brandl et al. 2006), local ULIRGs from the bright *IRAS* sample (Armus et al. 2006, 2007) and high-redshift mid-IR-selected sources (Sajina et al. 2007). We see that SMGs are among the most PAH-luminous objects in the universe, with PAH features nearly four and two orders of magnitude more luminous than local starbursts and local ULIRGs, respectively. This means that the SMG population comprises the most vigorous star-formation events ever observed. See §3.4.2.

environments within SMGs. Fig. 3.9 illustrates that the distribution in values for the 7.7/11.3 PAH ratio in SMGs is very broad and extends over a similar range to that of the high-redshift 24μm-selected sources studied by Sajina et al. (2007). We also compare to the nuclear starburst galaxies from Brandl et al. (2006) and find that SMGs have a median 7.7/11.3 PAH ratio similar to that of low-redshift nuclear starbursts (3.7 ± 1.7 versus 3.7 ± 0.9). Such diversity in PAH ratios is also present in local ULIRGs (e.g., Rigopoulou et al. 1999; Peeters et al. 2004), indicating that diverse radiation field strengths are found amongst both low- and high-redshift sources. However, we note that the need for measurable 11.3 μm emission means that this comparison only includes SMGs at $z < 1.6$ (Fig. 3.4).

Fig. 3.9 also shows that the bulk of SMGs have 7.7/6.2 PAH ratios that are lower than both the high-redshift sources in Sajina et al. (2007) and the median value found for local nuclear starbursts (2.5 ± 1.4 for SMGs versus 5.3 ± 1.7 for the starbursts). This suggests that an intrinsic difference in either radiation field or extinction exists between SMGs and low-redshift nuclear starbursts, which results in a suppressed 6.2 μm PAH feature (Rigopoulou et al. 1999) and a relatively prominent 7.7 μm PAH feature. As we discuss in §3.5.2, we believe that a lesser degree of extinction is responsible for this behavior in SMGs.

3.4.3 Continuum Slopes

The continuum power-law index $\alpha_{\rm MIR}$ characterizes the steepness of the mid-IR continuum, although it requires adequate wavelength coverage to be measured reliably. In Table 3.4 we present the $\alpha_{\rm MIR}$ values for the SMGs whose spectra cover a wavelength range that extends longwards of the silicate absorption and that we thus consider reliable. We find that the SMGs in our sample have a median mid-IR power-law index of $\alpha_{\rm MIR} = 1.3 \pm 1.1$, typical of the continuum found for star-forming regions. The individual spectra span a range of power-law indices $\alpha_{\rm MIR} \sim -0.6$–$2.5$. The majority of our sample, 9/14 SMGs or $\sim 65\%$, have power-law indices which are characteristic of star forming regions ($\alpha_{\rm MIR} \gtrsim 0.5$). The remaining 35% (5/14) have $\alpha_{\rm MIR} \lesssim 0.5$

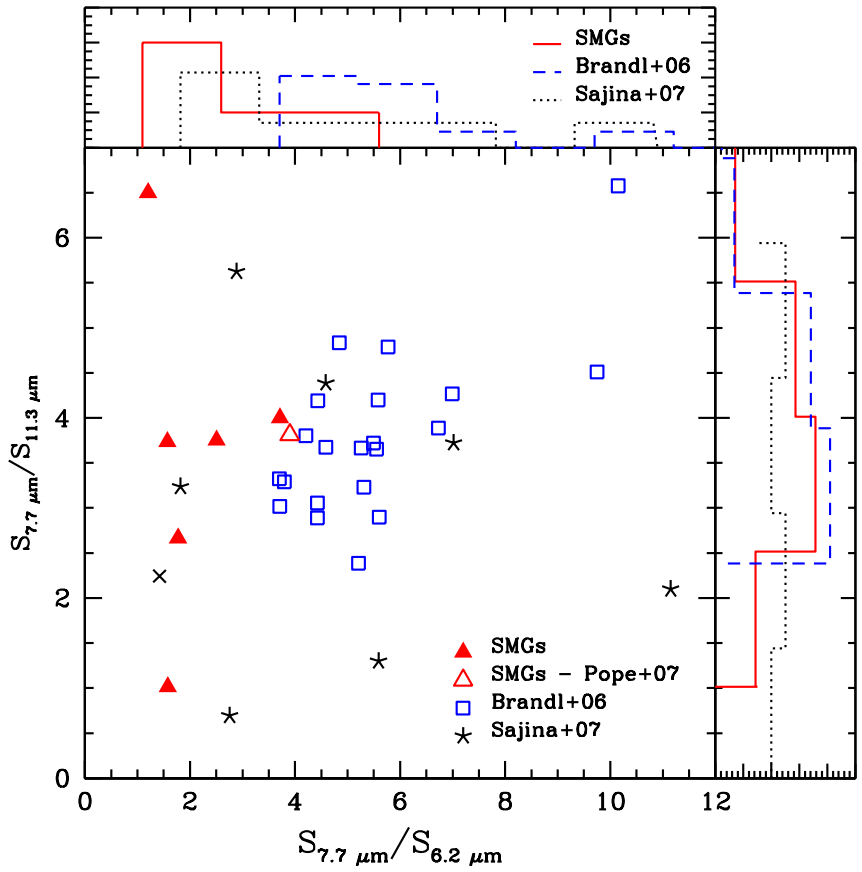

Figure 3.9 PAH ratios for the SMGs in our sample. We also include PAH ratios measured for a sample of low-redshift nuclear starbursts (Brandl et al. 2006), and high-redshift mid-IR selected sources (Sajina et al. 2007). SMGs have similar 7.7/11.3 PAH ratios to these two populations and the distribution of 7.7/6.2 PAH ratios occupies the same range as high-redshift mid-IR selected sources. However, SMGs display 7.7/6.2 PAH ratios that are in general lower than that of low-redshift starbursts.

more characteristic of AGN-dominated regions (e.g., Deo et al. 2007).

For a subset of our sample (those at $z < 1.6$) we can also characterize the continuum shape in the SMGs from their $S_{6\mu m}/S_{12\mu m}$ colors, which is measured at wavelengths devoid of substantial contamination from PAH emission. At 6 μm, the continuum traces thermal emission from hot ($T_{dust} \sim 500$ K) dust, while at 12 μm, the continuum is dominated by dust heated to lower temperatures ($T_{dust} \sim 250$ K). We find that the 4/7 ($\sim 60\%$, Table 3.4) of the SMGs for which we can determine their mid-IR colors show red continua ($S_{6\mu m}/S_{12\mu m} \lesssim 0.3$, $\alpha_{\rm MIR} \gtrsim 0.5$) which resemble the

colors of low-redshift star-forming galaxies and the nuclear starburst galaxies presented by Brandl et al. (2006): $S_{6\mu m}/S_{12\mu m} \sim 0.18$–$0.53$. The remaining 40% of this subsample have bluer continua ($S_{6\mu m}/S_{12\mu m} \gtrsim 0.3$, $\alpha_{\rm MIR} \lesssim 0.5$), more typical of the high-redshift mid-IR selected sources of Sajina et al. (2007) with $S_{6\mu m}/S_{12\mu m} \gtrsim 0.3$.

Taken together, these results suggests that the mid-IR continuum emission in the two-thirds of the SMGs in our sample has the spectral characteristics associated with star forming systems locally. The remaining third of the SMGs show more AGN-like mid-IR continua, although these frequently also display strong PAH emission.

3.4.4 Obscuration as Measured by silicate Absorption

One of the clearest indicators of absorption in the mid-IR arises from intervening amorphous silicate dust grains. Silicate absorption from the stretching of Si-O bonds centered around 9.7 μm is the main absorption feature within the wavelength range considered in this work and is measurable in roughly half of the SMGs in our sample, those at $z < 2.0$.

We use the strength of the silicate-absorption feature as a measure of the obscuration along the line of sight to the warm continuum emission, $\tau_{9.7\mu m}$. We note that this definition of optical depth assumes that the obscuring material lies in a foreground screen, which is likely to be too naive a model for the complex spatial mix of absorption and emission in SMGs.

To calculate $\tau_{9.7\mu m}$ for the individual SMGs, we assume that the bottom of silicate absorption feature is well constrained. However, we stress that since we only detect faint continuum with $S/N \lesssim 3$ for a number of SMGs in our sample, the values we derive for the strength of the silicate absorption are likely lower limits (see Table 3.2). We find a range of optical depths $\tau_{9.7\ \mu m} \sim 0.05$–$1.2$ for the SMGs in our sample, with a median value of $< \tau_{9.7\mu m} >= 0.3 \pm 0.1$.[11] For the composite spectrum, which benefits from an improved S/N, we find an optical depth of $\tau_{9.7\ \mu m} = 0.44 \pm 0.06$.

In Fig. 3.10 we compare the optical depths in SMGs to those of low-redshift nuclear

[11]Including the SMGs with redshifts from C05 from Pope et al. (2008) extends this range to $\tau_{9.7\ \mu m} \sim 1.4$.

starbursts and ULIRGs and to high-redshift mid-IR selected sources. We find that the bulk of SMGs have $\tau_{9.7\ \mu\mathrm{m}}$ values that extend across the range of values covered by high-redshift mid-IR selected sources, but are typically less than those seen in local nuclear starbursts or local ULIRGs. This suggests that the SMGs have lower typical extinction along the lines of sight to their warm continuum emission sources. We stress that the IRS observations of the local ULIRG sample contain 80–90% of the star-formation activity in these systems falling in the slit, and hence these differences in apparent optical depth are not due to comparing galaxy-integrated measurements for the SMGs to measurements of just the nuclear component in local systems (Armus et al. 2007).

We also explore in Fig. 3.10 the distribution in $\tau_{9.7\ \mu\mathrm{m}}$ as a function of the 7.7 μm PAH luminosity relative to the hot-dust continuum at 6 μm, $L_{7.7}/L_6$. The distribution in $(L_{7.7}/L_6)$-values for SMGs and low-redshift star-forming galaxies is quite similar ($L_{7.7}/L_6 \sim 0.1 - 0.8$), and separates from the mid-IR bright high-redshift sources, which display lower values ($L_{7.7}/L_6 \lesssim 0.4$).

3.4.5 Composite Spectra of SMG subsets

3.4.5.1 Investigating 24 μm Selection Biases

We investigate the differences between 24μm-bright and 24μm-faint SMGs (in the observed frame) to understand how representative our sample is of the bulk of the SMG population which have counterparts which are faint at 24 μm. Using the SMGs within the $L_{8\ \mu\mathrm{m}}$-complete sample described in §3.3.1 (see Fig. 3.5), we construct mid-IR composite spectra based on 24 μm-brightness: SMGs with $S_{24\ \mu\mathrm{m}} \gtrsim 0.4\,\mathrm{mJy}$ comprise the 24μm–bright composite, while those with $S_{24\ \mu\mathrm{m}} \lesssim 0.4\,\mathrm{mJy}$ make up the 24μm–faint composite (see Fig. 3.11).

We see stronger 7.7 μm PAH emission, as demonstrated by the line's EW (see Table 3.3), in the 24μm–faint composite, while the 24μm–bright composite displays a greater contribution from hot dust continuum. Thus it appears that the strong PAH emission we see in our SMG sample at $z \sim 2$ is not likely to be a result of our use

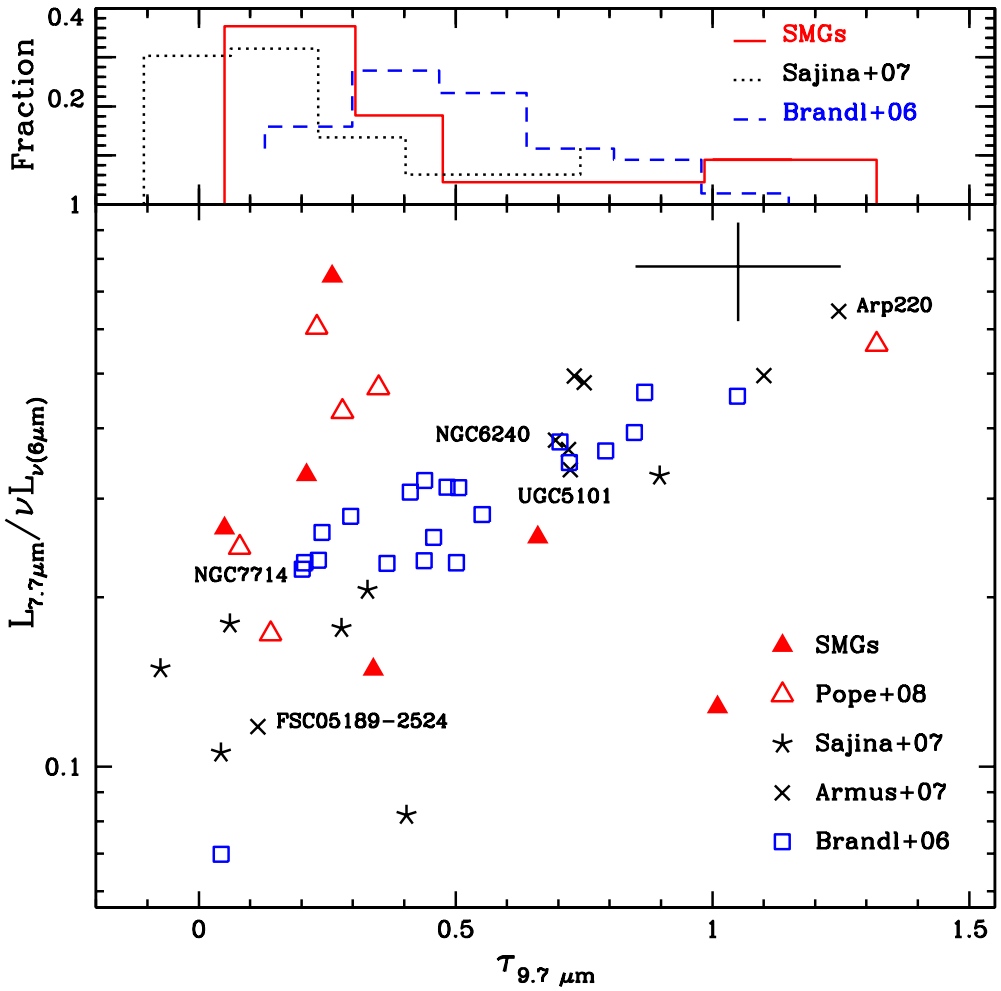

Figure 3.10 A plot of the 7.7 μm PAH luminosity relative to the 6 μm continuum luminosity as a function of silicate optical depth. We include only those SMGs that provide sufficient wavelength coverage for reasonable continuum estimates: 10 SMGs from our sample and seven SMGs from Pope et al. (2008). Optical depths for local nuclear starbursts (Brandl et al. 2006), local ULIRGs (Armus et al. 2007) and high-redshift 24μm-selected sources (Sajina et al. 2007) are also shown for comparison. The error bar displays the representative uncertainties in these measurements. The histogram at the top shows the cumulative distributions for the three samples. We see that the SMGs display much weaker silicate absorption than local nuclear starbursts and ULIRGs, but proportionally stronger 7.7 μm PAH emission. This suggests that the activity in these systems is occurring in less intense environments, even though the SMGs have integrated star-formation rates some four orders of magnitude higher than the local starbursts.

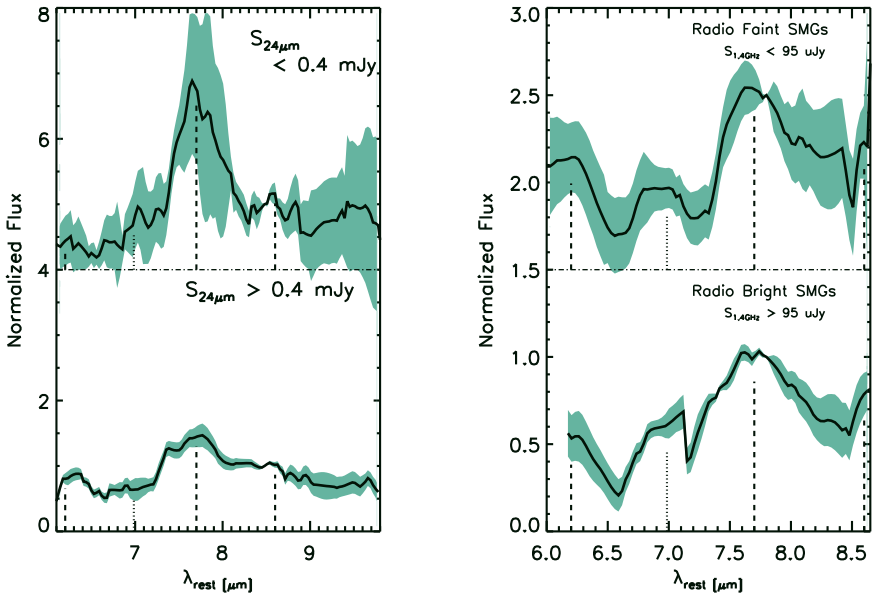

Figure 3.11 (**Left:**) The composite spectra of the seven 24 μm-bright SMGs (bottom) and of the seven 24 μm-faint SMGs (top) within the $L_{8\mu m}$-complete sample. (**Right:**) Composite spectra of the five radio-bright SMGs (top) and of the five radio-faint SMGs (bottom) within the $L_{1.4GHz}$-complete sample. Note that the spectra of the individual SMGs that comprise the radio composites are normalized by their flux at $\lambda = 7.8$ μm. The same flux-scale is maintained for the spectra within each panel and the dash-dotted line denotes the offset zero level for the 24 μm-faint and radio-faint composites. We see that 24μm-faint composite is significantly more PAH-dominated than the 24μm-bright composite, while the latter displays a stronger continuum. In the case of the radio-composites, the radio-bright sample displays a broader 7.7 μm PAH feature over a slightly more prominent continuum. The characterization of the radio-composite spectra do not reveal any significant difference within our measurement uncertainties (see Table 3.3).

Table 3.3. Composite Spectra

Composite	# SMGs	z_{median} [a]	$L_{6.2}$ [b]	$EW_{6.2}$ [c]	$L_{7.7}$	$EW_{7.7}$	$L_{11.3}$	$EW_{11.3}$	$S_{6\mu m}/S_{12\mu m}$	$\alpha_{\rm MIR}$	$\tau_{9.7\mu m}$
all	22	2.00	0.50 ± 0.01	0.05 ± 0.01	3.57 ± 0.05	0.42 ± 0.02	1.16 ± 0.04	0.19 ± 0.02	0.34 ± 0.07	1.17 ± 0.11	0.44 ± 0.06
24um-Bright[d]	7	2.10	–	–	3.51 ± 0.05	0.32 ± 0.01	–	–	–	–	–
24um-Faint[e]	7	2.61	–	–	10.67 ± 0.06	0.69 ± 0.01	–	–	–	–	–
Radio-Bright[f]	5	3.04	–	–	3.67 ± 0.22	0.17 ± 0.04	–	–	–	–	–
Radio-Faint[g]	5	2.38	–	–	1.92 ± 0.11	0.17 ± 0.03	–	–	–	–	–
Starburst-dominated (Xray/UV/opt)[h]	16	1.98	0.59 ± 0.02	0.06 ± 0.01	5.46 ± 0.11	0.70 ± 0.04	1.87 ± 0.15	0.44 ± 0.10	0.41 ± 0.11	0.46 ± 0.07	0.21 ± 0.05
Starburst-dominated (mid-IR)[i]	12	1.97	1.02 ± 0.02	0.09 ± 0.02	5.04 ± 0.11	0.63 ± 0.04	2.09 ± 0.12	0.49 ± 0.08	0.36 ± 0.15	0.40 ± 0.06	0.48 ± 0.10
AGN (Xray/UV/opt)[j]	8	2.00	2.36 ± 0.08	–	3.23 ± 0.15	0.42 ± 0.06	1.66 ± 0.09	0.37 ± 0.02	0.46 ± 0.18	0.59 ± 0.08	0.26 ± 0.04
AGN (mid-IR)[k]	10	2.02	0.75 ± 0.03	–	4.62 ± 0.13	0.52 ± 0.04	1.53 ± 0.10	0.31 ± 0.06	0.44 ± 0.26	0.50 ± 0.06	0.02 ± 0.01

[a] Median redshift of SMGs comprising composite spectrum.

[b] PAH luminosities are expressed in units of $10^{44}\,{\rm erg\,s^{-1}}$. Uncertainties are derived from the propagation of integrated line flux uncertainties as determined by our PAH fitting approach. An additional $\sim 20\%$ is attributed to flux calibration and continuum determination.

[c] PAH rest-frame EWs are expressed in units of [μm].

[d] $S_{24\mu m} > 0.40\,{\rm mJy}$ from the 8μm luminosity-complete sub-sample of SMGs with $L_{8\mu m} > 10^{32}\,{\rm erg\,s^{-1}}$

[e] $S_{24\mu m} < 0.40\,{\rm mJy}$ from the 8μm luminosity-complete sub-sample of SMGs with $L_{8\mu m} > 10^{32}\,{\rm erg\,s^{-1}}$

[f] $S_{1.4GHz} > 95\mu$Jy from the luminosity-complete sub-sample of SMGs with $L_{1.4GHz} > 2 \times 10^{24}\,{\rm erg\,s^{-1}\,Hz^{-1}}$

[g] $S_{1.4GHz} < 95\mu$Jy from the luminosity-complete sub-sample of SMGs with $L_{1.4GHz} > 2 \times 10^{24}\,{\rm erg\,s^{-1}\,Hz^{-1}}$

[h] Composite of SMGs classified as starburst-dominated in the rest-frame optical (Swinbank et al. 2004; Takata et al. 2006), UV (C05) and/or X-ray (Alexander et al. 2005a)

[i] Composite of SMGs classified as starburst-dominated in the mid-IR, with $EW_{7.7\mu m} > 1$ and $\alpha_{\rm MIR} > 0.5$. See text for details.

[j] Composite of SMGs with AGN signatures in the X-ray (Alexander et al. 2005a) and/or in the near-IR (Swinbank et al. 2004; Takata et al. 2006)

[k] Composite of SMGs with AGN signatures in the mid-IR: $EW_{7.7\mu m} < 1$ and $\alpha_{\rm MIR} < 0.5$. See text for details.

of estimated 24 μm-fluxes in selecting our sample, although the prevalence of sources with strong continuum emission (and hence the contribution from AGN or highly obscured starbursts) is likely to be higher in our sample than in the general SMG population.

3.4.5.2 Exploring the Radio Bias

We use the range in radio fluxes covered by our sample (see Fig. 3.1) to investigate possible intrinsic trends in mid-IR properties associated with radio brightness. We seek to address potential differences between our sample of radio-identified SMGs and the $\lesssim 30\%$ of $S_{850\mu\mathrm{m}} \gtrsim 5\,\mathrm{mJy}$ SMGs with radio counterparts below the sensitivity of current radio surveys. The lack of a radio counterpart for an SMG may result from their lying at significantly higher redshifts than the radio-identified population ($z \gg 3$, C05; Younger et al. 2007). We cannot test this suggestion with our sample as we have targeted SMGs with known redshifts. However, it has also been suggested that the radio-undetected SMGs lie at similar redshifts to the dominant radio-detected population, but that they have somewhat lower IR luminosities and slightly colder characteristic dust temperatures, a combination which would result in similar observed 850 μm fluxes (Blain et al. 1999; Chapman et al. 2004). Our radio-detected sample may therefore be biased towards systems with hotter characteristic dust temperatures, either due to typically more compact star forming regions or the presence of an AGN. To investigate this possibility, we divide our sample into radio-bright and radio-faint SMGs. We first define a luminosity-complete sub-sample of SMGs based on their rest-frame radio luminosity and use their apparent radio fluxes to build the composite spectra (see Fig. 3.11).

The radio-faint SMG composite has a narrow 7.7 μm PAH feature that emerges sharply from the continuum, while the radio-bright composite displays a broader, less distinct PAH feature. Considering the line-to-continuum parameter (l/c; e.g., Genzel et al. 1998), traditionally used to gauge the strength of PAH features, the radio-faint composite displays a higher 7.7 μm–(l/c) relative to the radio-bright composite. This difference may suggest that the radio-bright composite has a larger obscured AGN

contribution, which we perceive in the mid-IR as a broadening of the 7.7 μm PAH feature, which could ultimately become a continuum-dominated feature at $\lambda \sim 8$ μm, similar to the spectrum of SMM J163650.43. However, the EWs of the 7.7 μm PAH feature in these composites are not significantly different within the measurement uncertainties (see Table 3.3). Therefore, overall our observations do not reveal any significant difference in mid-IR properties based on radio-luminosity and we conclude that our radio-detected SMG sample is likely to be representative of the whole SMG population at $z \lesssim 3.5$.

3.4.5.3 Starburst and AGN-Dominated Composites

The SMGs in our sample have been classified prior to this work as either AGN- or star-formation–dominated systems using deep X-ray observations (Alexander et al. 2005a), rest-frame optical spectroscopy (Swinbank et al. 2004; Takata et al. 2006) and/or rest-frame UV spectroscopy (C05). Table 3.4 provides a summary of these classifications. We construct composites for an AGN and star-forming class based on these classifications to investigate differences in mid-IR spectral properties (see Fig. 3.12). Since we do not take mid-IR properties into account to build these composites, the differences are not the result of any mid-IR selection bias.

Both composite spectra display prominent PAH features, but the PAH emission in the AGN composite spectrum lies on top of a stronger continuum, in comparison to the star-forming composite: the 7.7 μm PAH feature EW of 0.42 ± 0.06 and 0.70 ± 0.04 respectively reflect this difference. The other possible difference between these composites is that the AGN composite spectrum has an emission feature at $\lambda = 10.51$ μm, which is much less obvious in the star-forming composite. This feature may correspond to [SIV] narrow-line emission, which is commonly associated with a hot starburst or AGN activity (Spoon et al. 2002; Ogle et al. 2006). We note that all of the individual SMGs in this AGN-composite whose spectra cover the $\lambda \sim 10.5$ μm wavelength region show what could correspond to [SIV] emission (see Fig. 3.2). Since the SMGs that make up this composite have AGN signatures in the rest-frame UV and optical, it is likely that our line of sight has direct access into the broad line

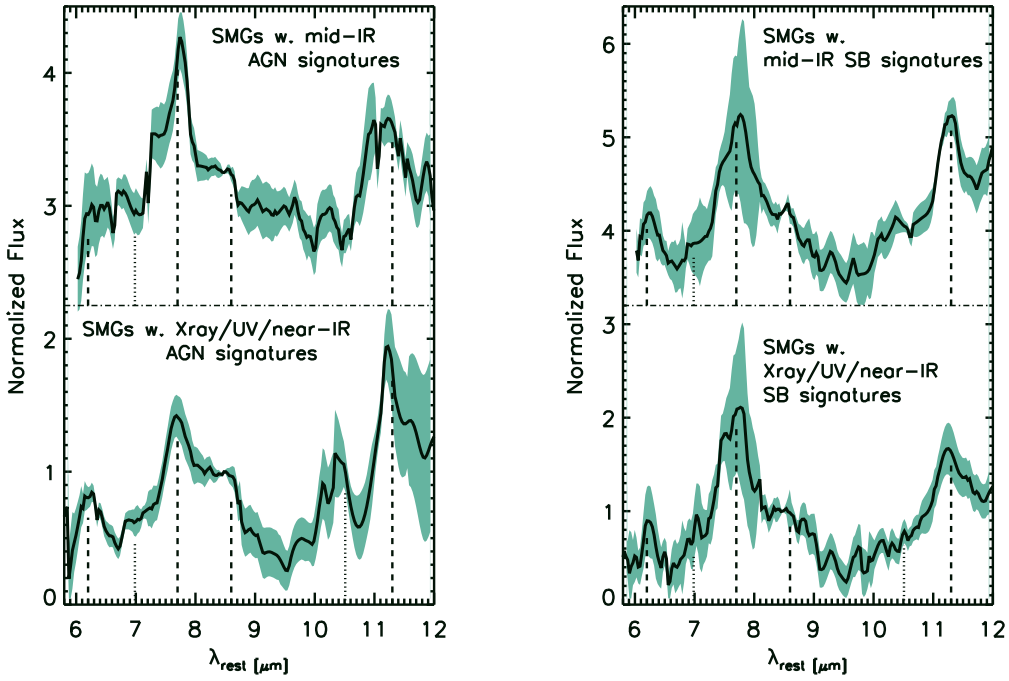

Figure 3.12 (**Left:**) Composite mid-IR spectra of the eight SMGs in the sample with AGN signatures in the X-ray (Alexander et al. 2005a), optical (C05) or near-IR (Swinbank et al. 2004) (bottom) and of the 10 SMGs with mid-IR spectra that suggest the presence of an AGN (top). (**Right:**) Composite spectra of the 16 SMGs in our sample with *no* AGN signature either in the X-ray, optical or near-IR (bottom) and of the 12 SMGs with mid-IR spectra dominated by strong star-formation activity. We see that the AGN-composites display an enhanced continuum relative to the star-forming counterparts. We also note that the AGN-composite with AGN signatures at wavelengths other than the mid-IR (bottom left panel) displays a prominent emission feature, likely corresponding to [SIV] emission from an AGN. See §3.4.5.3 for details.

region. Thus it is also possible that this feature corresponds instead to solid silicate emission from very near a central AGN.

In Fig. 3.12 we show the composite spectra for AGN- and starburst- subsets, based this time on their mid-IR classifications. We classify SMGs with $\mathrm{EW}_{7.7\ \mu\mathrm{m}} \gtrsim 1$ or steep mid-IR continua ($S_{6\ \mu\mathrm{m}}/S_{12\ \mu\mathrm{m}} \lesssim 0.3$) as star-formation–dominated systems; SMGs with $\mathrm{EW}_{7.7\ \mu\mathrm{m}} \lesssim 1$ or flat mid-IR continua ($S_{6\ \mu\mathrm{m}/12\ \mu\mathrm{m}} \gtrsim 0.8$ or $\alpha_{\mathrm{MIR}} \lesssim 0.5$) are classified as having a significant AGN contribution (see Table 3.4). Both of these composites display an enhanced underlying continuum, relative to their respective composite counterparts based on AGN signatures at other wavelengths. This is most likely due to the need to have moderate mid-IR emission for an object to be classifiable in the mid-IR. However, there is one notable difference between the two mid-IR classified spectra: Fig. 3.12 shows that the 6.2 μm PAH feature appears to have been diluted by the enhanced continuum in the AGN composite.

3.4.6 The SMG Spectrum

With more than $\sim 80\%$ of the individual SMGs in our sample displaying PAH features, unsurprisingly the composite spectrum in Fig. 3.4 displays prominent PAH emission. Using our large sample of SMGs covering a wide redshift range, we explore composite spectra of SMGs in three redshift bins: low ($z \leq 1.6$), intermediate ($z = 1.6$–2.4) and a high ($z \geq 2.4$); see Fig. 3.4. The SMGs in the low-redshift bin dominate the composite spectrum at $\lambda \gtrsim 10$ μm. All three redshift composites display strong 7.7 μm PAH emission and a prominent 8.6 μm feature. With increasing redshift we observe a broadening of the 7.7 μm PAH feature and a weakening of the 6.2 μm PAH feature. The increase in scatter around the median composite spectrum indicates either a more diverse range in spectral properties at the higher redshifts, or poorer S/N. However, we note that the three composites display an increase in continuum level with redshift. Within the context discussed in §3.4.2, the weakening of the observed 6.2 μm PAH emission feature may be an indication that SMGs at higher redshifts suffer from either increased extinction, hampering detection of PAH emission

features at the shorter wavelengths, or from a systematic hardening of the radiation field that the PAH molecules encounter.

3.4.6.1 Comparison to Local Templates

In Chapter 2 (Menéndez-Delmestre et al. 2007) we found that the composite spectrum is well fit by a starburst-like template (represented by M82) with an additional continuum component, likely arising from an AGN (see Fig. 2.1). We found that the mid-IR spectral features of SMGs are more comparable to those of the M82 starburst, than to other well-studied local ULIRGs, such as Arp 220 and Mrk 1014. We now consider our complete sample of 24 SMGs.

The mid-IR composite spectrum of the SMGs in our sample is reasonably well fit at $\lambda \lesssim 10$ μm by the composite spectrum of nearby nuclear starburst-dominated galaxies (Brandl et al. 2006; see Fig. 3.13). By using this more diverse starburst template, we seek to better represent the diversity in continuum slopes and PAH strengths in starburst-dominated galaxies in the local Universe.

The PAH component of the SMG composite spectrum is well represented by a starburst template, but we find that an additional power-law continuum remains necessary to describe the overall composite spectrum: at the longer wavelengths, $\lambda \gtrsim 10$ μm, the starburst template fails to match the continuum level (see Fig. 3.13). This continuum component may be associated with AGN activity or an additional starburst continuum component. To quantify this we characterize the red continuum in the composite SMG that is unaccounted for by the starburst template by fitting a power-law to the (SMG composite − starburst-template) residuals. We find that the residuals are best fit by a power-law $F_\nu \sim \nu^{-\alpha_{\rm MIR}}$, where $\alpha_{\rm MIR} = 1.97 \pm 0.22$. In the next section we estimate an upper limit to the contribution from an AGN, making the conservative assumption that all of the additional continuum component arises from a dust-enshrouded AGN.

Table 3.4. AGN and Starburst Signatures in Radio-Identified SMGs

SMM J	$\alpha_{\rm MIR}$[a]	$S_{6.0}/S_{12.0}$	X-ray[b]	UV[c]	Hα	mid-IR	Comment
030227.73	2.08 ± 0.11	0.24 ± 0.12	–	SB	AGN[d,e]	int	$\alpha_{\rm MIR} > 0.5$, EW$_{7.7\mu m} < 1$
030231.81	–	–	–	SB	–	–	undetected
105151.69	0.07 ± 0.22	0.96 ± 0.48	–	SB	–	int	$\alpha_{\rm MIR} < 0.5$, EW$_{7.7\mu m} < 1$
105158.02	–	–	–	SB	SB[d]	SB?	strong PAH emission above faint continuum
105200.22	1.76 ± 0.11	0.30 ± 0.14	–	SB	–	SB	$\alpha_{\rm MIR} > 0.5$
105227.58	–	–	–	SB	–	int	EW$_{7.7\mu m} < 1$
105238.19	–	–	–	SB	–	SB	EW$_{7.7\mu m} > 1$
105238.30	–	–	–	AGN	–	AGN	EW$_{7.7\mu m} < 1$, continuum-dominated
123549.44	–	–	AGN	SB	int[d]/AGN[e]	int	EW$_{7.7\mu m} < 1$
123553.26	−0.75 ± 0.50	–	SB	SB	–	AGN	$\alpha_{\rm MIR} < 0.5$, EW$_{7.7\mu m} < 1$, continuum-dominated
123707.21	2.46 ± 1.3	–	AGN	SB	SB[e]	int	EW$_{7.7\mu m} < 1$
123711.98	−0.10 ± 0.30	<1.07	AGN	SB	–	int	$\alpha_{\rm MIR} < 0.5$, EW$_{7.7\mu m} > 1$, faint continuum
123721.87	0.22 ± 0.33	<0.86	AGN	AGN	SB[e]	int	EW$_{7.7\mu m} < 1, \alpha_{\rm MIR} < 0.5$
163639.01	2.20 ± 0.32	<0.22	–	SB	SB[d]/int[e]	int	EW$_{7.7\mu m} < 1, \alpha_{\rm MIR} > 0.5$
163650.43	–	–	–	int	AGN[d,e]	AGN	Absorbed continuum
163658.78	2.07 ± 0.32	0.24 ± 0.06	–	SB	–	SB	$\alpha_{\rm MIR} > 0.5$, EW$_{7.7\mu m} \sim 1$
221733.02	−0.62 ± 0.45	–	–	SB	SB[e]	int	$\alpha_{\rm MIR} < 0.5$, prominent 7.7μm PAH feature
221733.12	1.26 ± 0.25	–	–	SB	–	SB	$\alpha_{\rm MIR} > 0.5$, prominent 11.3, 12.7μm PAH features
221733.91	0.84 ± 0.72	–	–	SB	SB[d]	int	$\alpha_{\rm MIR} > 0.5$, EW$_{7.7\mu m} < 1$
221735.15	–	–	–	SB	–	–	EW$_{7.7\mu m} < 1$, faint continuum
221735.84	–	–	–	SB	–	–	7.7μm PAH feature above faint continuum
221737.39	–	–	–	SB	AGN[e]	AGN	featureless, continuum-dominated
221804.42	–	–	–	SB	–	SB?	EW$_{7.7\mu m} > 1$, faint continuum
221806.77	−0.39 ± 0.35	–	–	SB	–	int	EW$_{7.7\mu m} < 1$, $\alpha_{\rm MIR} < 0.5$

[a] We report mid-IR colors for SMGs with wavelength coverage $\lambda_{rest} \sim 6$–12μm.

[b] From Alexander et al. (2005a)

[c] From C05

[d] From Swinbank et al. (2004)

[e] From Takata et al. (2006)

3.4.7 The AGN Contribution to the Bolometric Luminosity in SMGs

Hard X-ray emission provides one of the most direct routes to estimate the luminosities of AGN. However, in the presence of high column densities, such as are found for SMGs ($N_H \sim 10^{23}$–$10^{24}\,cm^{-2}$; Alexander et al. 2005a,b), hard X-ray photons may be completely absorbed. In these difficult cases an alternate probe for AGN emission is to trace the mid-IR emission from hot dust near the AGN. The mid-IR thus provides a complementary insight into a deeply obscured AGN (Sturm et al. 2006; Lutz et al. 2004). In particular, Krabbe et al. (2001) show that the 10.5 μm-flux is tightly correlated with the moderately hard X-ray emission, $S_{2-10keV}$, both in Seyfert and in starburst galaxies, which have markedly distinct mid-IR slopes. We use the derived correlation for Seyfert galaxies to estimate the X-ray luminosity of the AGN component in the SMG composite spectrum and thus estimate the AGN contribution to the bolometric luminosity of SMGs.

The composite spectrum includes a power-law continuum, $S_\nu \sim \nu^{-\alpha_{MIR}}$, with spectral slope $\alpha_{MIR} = 1.97 \pm 0.22$ (see Fig. 3.13). From the 10.5 μm continuum flux we infer an X-ray luminosity, $L_X \sim 8 \times 10^{43}\,erg\,s^{-1}$, for the SMGs in our sample at $< z > \sim 2.0$. Encouragingly, this estimate is in close agreement with the absorption corrected rest-frame 0.5–8 keV X-ray luminosities found for the SMGs in the *Chandra* Deep Field (Alexander et al. 2005a), $< L_X >= 5 \times 10^{43}$ erg s^{-1}. To assess the contribution of the AGN to the energetics of the SMGs we first estimate the far-IR luminosities of the SMGs using the observed radio–far-IR correlation for SMGs (Kovács et al. 2006), yielding an average far-IR luminosity of $L_{IR} \sim 5 \times 10^{45}\,erg\,s^{-1}$. We then use the approach of Alexander et al. (2005a) and Menéndez-Delmestre et al. (2007), adopting the X-ray-to-FIR luminosity ratio typically found for quasars ($L_X/L_{IR} \simeq 0.05$; Alexander et al. 2005a) to estimate that the AGN in SMGs contribute $L_{IR} \simeq 1.6 \times 10^{45}$ erg s^{-1}, or $\lesssim 35\%$ of the SMG's far-IR luminosities. As discussed earlier, due to the biases towards including mid-IR bright SMGs in our sample, it is likely that the AGN contribution estimated here is biased high. It is also

very likely that some fraction of this red continuum arises from dust emission heated by very deeply enshrouded starbursts in these SMGs and so we claim this as a firm upper limit to the AGN contribution in typical SMGs.

With an SMG composite dominated by PAH features, it is clear that the bolometric luminosity of SMGs is in general dominated by star formation. However, the individual mid-IR SMG spectra display modest variation in AGN contribution and in some cases reveal the presence of an AGN that remains invisible at other wavelengths (see Table 3.4). In particular, there is evidence that SMM J123553.26 is a Compton-thick AGN: it is undetected in the X-ray but is bright and dominated by continuum emission in the mid-IR and displays no mid-IR signatures of star formation (see Fig. 3.2). Extrapolating from its mid-IR spectrum, we estimate a hot dust luminosity [12], $L_{6\mu\mathrm{m}} \sim 2.0 \times 10^{45}$ erg s^{-1}. Following the procedure described by Alexander et al. (2008b) we use the 0.5–2 keV observed luminosity for SMM J123553.26 (Alexander et al. 2005a) to derive a rest-frame 1.6–24.8 keV luminosity, which we convert to an intrinsic X-ray luminosity, $L_{2-10\mathrm{keV}} < 2 \times 10^{42}$ erg s^{-1}, assuming an X-ray spectral index, $\Gamma = 1.4$. On the basis of the X-ray-to-6μm luminosity ratio of this SMG, we find that it lies significantly below the X-ray-to-6μm luminosity relationship found for nearby AGN, suggesting that this source hosts a luminous Compton-thick AGN (e.g., Alexander et al. 2008b). However, we note that this SMG lies very close to a number of mid-IR bright sources, which complicates the deblending of the individual flux contributions in MIPS 24 μm imaging (Hainline et al. 2009). We detect only a single source in the IRS 2D spectrum. While this coincides with the position expected for SMM J123553.26, it remains possible that the measured mid-IR flux of this source does not correspond to the X-ray source.

3.4.8 Comparison to SMGs in Other Samples

With a sample of 23 detected SMGs in this work, plus nine from Valiante et al. (2007) and 13 from Pope et al. (2008), we have statistics to allow an adequate eval-

[12] $\nu\,\mathrm{L}_\nu = 4\pi D_L^2 S_{6\mu\mathrm{m}} \times \nu_{6\mu\mathrm{m}}/(1+z)$

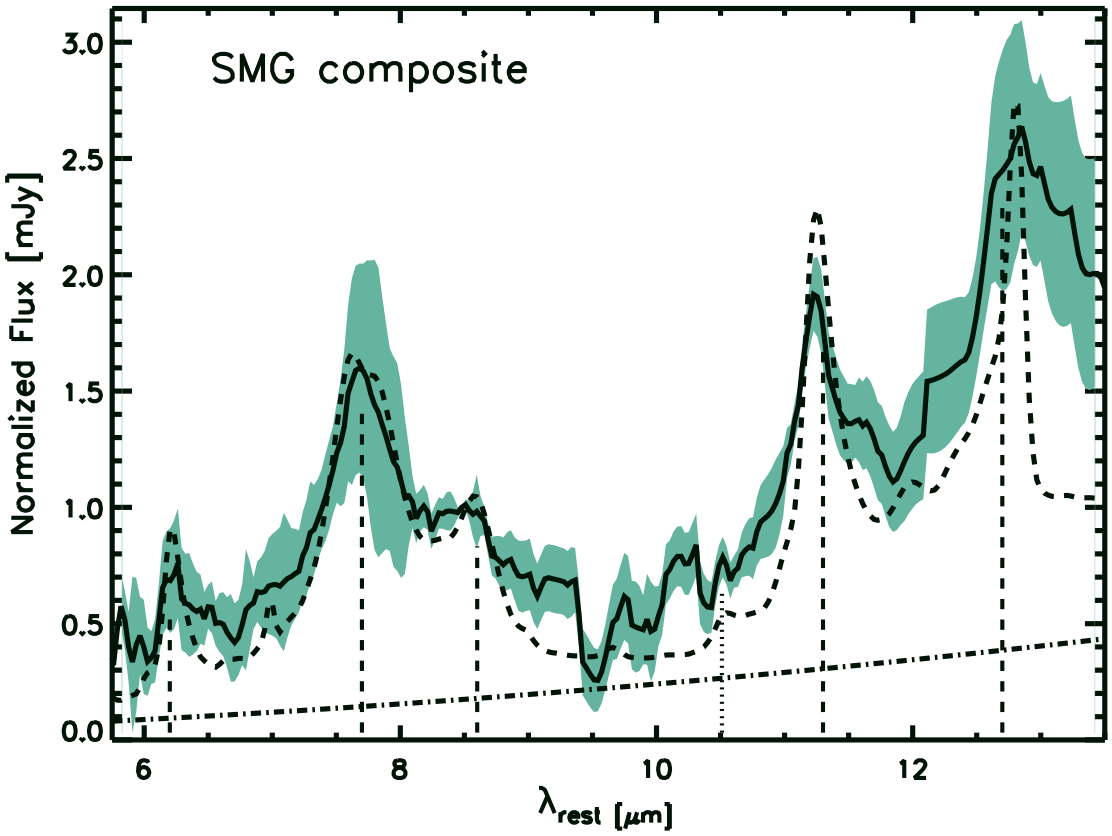

Figure 3.13 The composite spectrum of 22 SMGs detected in our sample as shown in Fig. 3.4. The dashed curve is the mid-IR composite spectrum of 13 starburst-dominated low-redshift galaxies from Brandl et al. (2006), scaled down to match the SMG composite spectrum at 7.7 μm. The dash-dotted line is the power-law component ($\nu S_\nu \sim \nu^{-\alpha}$, $\alpha_{\rm MIR} \sim 1.97$) that best represents the continuum in the composite SMG that is unaccounted for by the starburst template. See § 3.4.7 for details.

uation of the mid-IR properties of the SMG population as a whole. The majority of SMGs display dominant PAH features atop an underlying power-law continuum, that potentially arises from an AGN.

Together with results published in parallel mid-IR studies (Lutz et al. 2005; Menéndez-Delmestre et al. 2007; Valiante et al. 2007; Pope et al. 2008), we are uncovering the range in mid-IR properties present within this galaxy population: mid-IR spectra that correspond to dominant starbursts, with varying AGN contributions to their bolometric luminosity. We find only one clear example of a continuum-dominated source with a prominent broad feature centered at $\lambda \sim 8$ μm, SMM J163650.43 (Menéndez-Delmestre et al. 2007). Three other SMGs in our sample display featureless continuum-dominated spectra (SMM J105238.30, SMM J123553.26, and SMM J221737.39). In the sample of nine detected SMGs presented by Valiante et al. (2007) and Lutz et al. (2005), SMM J02399-0136 displays PAH features overlaying a particularly strong continuum, and is thus classified as a source powered by equal contributions of star formation and a Compton-thick AGN (Valiante et al. 2007). Out of the 13 SMGs in the GOODS-North field, SMM J123600.15 (C1; Pope et al. 2008) also displays PAH features on a steeply rising continuum and is classified as an SMG with a 44% AGN contribution to the bolometric luminosity.

We note that 25% of the SMGs in our sample lie at redshifts $z \lesssim 1.2$, which is a redshift range not covered by the other SMG mid-IR studies. This extension to lower redshifts provides us with an extended insight into the longer mid-IR wavelengths, $\lambda \gtrsim 11.5$ μm, for a crucial comparison between SMGs and potential local analogs. This longer wavelength coverage is also very useful for constraining better the mid-IR continuum in these sources, and so for measuring features such as the 9.7 μm silicate absorption.

To determine explicitly the effect of including these longer wavelengths, we recalculated our results considering only the composite spectrum shortwards of $\lambda = 11.5$ μm. In this case, we find that the composite spectrum of the SMGs in our sample is well fit by the starburst template from Brandl et al. (2006) with an additional shallower continuum ($\alpha_{\rm MIR} \sim 0.94 \pm 0.31$), which translates into a $\lesssim 30\%$ AGN contribution. This

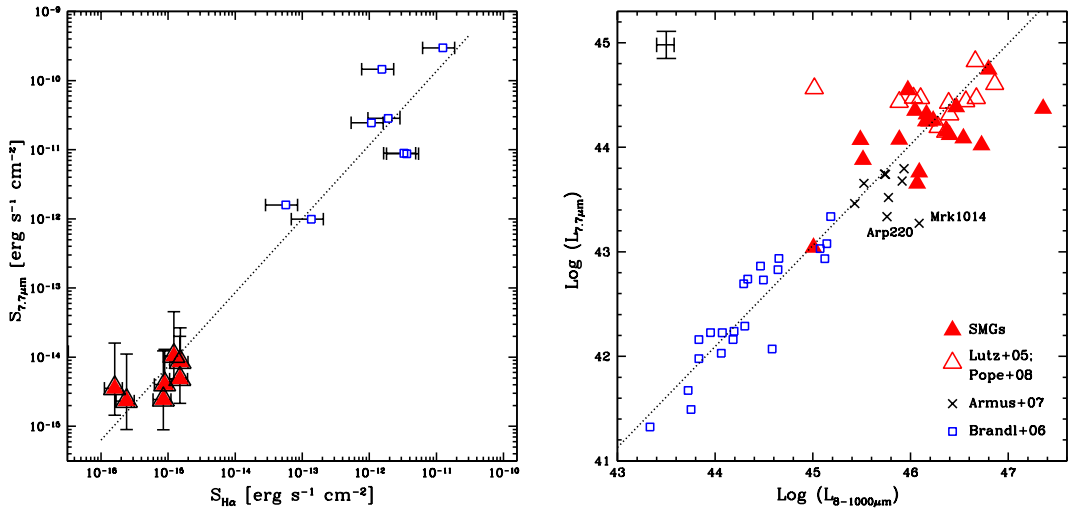

Figure 3.14 (**Left:**) The integrated flux of the 7.7 μm PAH feature as a function of narrow-line Hα flux for SMGs in our sample and for local galaxies. The Hα fluxes are corrected for extinction, typically by a factor of 2–3. Hα fluxes for the low redshift star-forming galaxies are taken from Armus et al. (1989), Heckman et al. (1990), Veilleux et al. (1999), Buat et al. (2002) and Lira et al. (2002). An uncertainty of $\sim 10\%$ is associated with the fluxes of the 7.7 μm PAH features for the low-redshift systems and this uncertainty is smaller than the points in the graph. The dotted line represents a simple best linear fit for both the low- and high-redshift samples, demonstrating the clear correlation between these parameters. We see that PAH integrated fluxes correlate well with narrow-line Hα and that SMGs extend the local relation out to the PAH- and Hα-bright region. (**Right:**) PAH luminosities as a function of IR luminosity for the SMGs in our sample and for those in Pope et al. (2008) and Lutz et al. (2005). We use total IR luminosities from C05, corrected by approximately a factor of two, following Kovács et al. (2006). We also include aperture-corrected PAH luminosities of low-redshift nuclear starbursts (Brandl et al. 2006) and local ULIRGs (Armus et al. 2007). The dotted line shows a simple best linear fit to local nuclear starbursts. The error bar represents the typical uncertainties in the observations.

power-law index is significantly lower than that corresponding to the best power-law fit determined for the full composite spectrum in Fig. 3.13, $\alpha_{\rm MIR} = 1.97 \pm 0.22$. The AGN contribution derived for the short-wavelength SMG composite is in agreement with the results of Pope et al. (2008), where the redshift range of the SMGs studied is restricted to $z \gtrsim 1.2$.

3.5 Discussion

We compare the mid-IR properties of the SMGs in our sample with those of starburst-dominated low-redshift galaxies (Brandl et al. 2006), select local ULIRGs from the Bright IRAS sample (Armus et al. 2006, 2007) and the mid-IR selected sources of Sajina et al. (2007). We use PAH luminosities, PAH relative intensities, the steepness of the continuum and the strength of silicate absorption to compare the level of star-forming activity, the energetics in radiation environments and the distribution of cold and warm dust in these galaxies.

SMGs have among the most luminous PAH emission of any population in the universe, displaying levels of activity which are unseen in local samples (Fig. 3.8). This result reflects the significant increase in star-formation activity in the high-redshift SMG population which underpins the thousand-fold increase in the space density of ULIRGs out to $z \sim 2$ (C05). A similar increase in PAH luminosity has been seen by Desai et al. (2007), who investigated the strength of the 6.2 μm PAH feature in ULIRGs at low and intermediate redshifts ($z \lesssim 1$) and found that ultra-luminous sources at high redshift have PAH EWs larger than any present in the local Universe.

We find that PAH luminosities display no dependence on continuum slope or continuum mid-IR color. Hot dust located close to an AGN would contribute to an enhanced continuum emission at the shorter mid-IR wavelengths ($\lambda \lesssim 10$ μm), and so we associate mid-IR spectra displaying flatter continua with the likely presence of an unobscured AGN. The presence of large PAH luminosities in SMGs with a flat mid-IR spectrum suggests that even in the presence of an AGN, PAH molecules are

abundant in these galaxies. Under the PAH *destruction* scenario (see Voit 1992), highly energetic photons from an AGN overcome the PAH binding energy, deplete the population of PAH molecules and thus reduce the observed PAH luminosity. Rather than a decrease in PAH luminosity, we find that SMGs with flatter continua generally have lower PAH EWs. Similar results have been recently discussed in the context of low-redshift ULIRGs by Desai et al. (2007), where a decrease in EWs for the 6.2 and 11.3 μm PAH features is observed with increasing 24 μm rest-frame luminosity. Together with these results, our findings suggest that an increase in the dust continuum dilutes the prominence of PAH features with respect to the local continuum. Our study allows us to extend the validity of this PAH-*dilution* scenario out to the higher redshifts of SMGs.

3.5.1 PAH Luminosities as a Star-Formation Rate Indicator

In Fig. 3.14 we compare the strength of the observed PAH features with familiar SFR indicators: Hα and the total IR-luminosity (Kennicutt 1998). In the past, authors have explored the use of the mid-IR light as a measure of galaxy SFRs. Elbaz et al. (2002) claim that the flux measured in the 6.75 μm *ISO* band is related to the total IR luminosity, which in the absence of an AGN is taken to be a good tracer of star-forming activity (Kennicutt 1998). Roussel et al. (2001) and Förster Schreiber et al. (2004) showed that there exists a correlation between *ISO* 6.75 μm light and Hα luminosity in local spirals and starburst galaxies. With the advent of much more sensitive Spitzer 8 μm IRAC results, Wu et al. (2005) and Alonso-Herrero et al. (2006) confirmed that the 8 μm band flux is closely associated with the star formation taking place in low-redshift ($z \lesssim 0.2$) luminous infrared galaxies with $L_{8-1000\ \mu\mathrm{m}} < 10^{12}\ \mathrm{L}_{\odot}$.

The interest in using the 7.7 μm PAH emission as a SFR indicator is that with it we are able to remove the continuum contribution to the 8 μm band, which in the presence of an AGN may be substantial and even dominant (see for example the continuum-dominated SMGs in Fig. 3.2: SMM J123553.26, SMM J163650.43 and SMM J221737.39). We find that the 7.7 μm PAH flux in SMGs correlates with the

extinction-corrected Hα flux (see Fig. 3.14). We emphasize that even though the same UV stellar radiation field is the source of excitation for the Hα and the PAH emission features, the excitation processes are quite distinct: Hα emission arises from ionized gas surrounding young O stars, while PAH emission is produced by the stochastic heating of very small dust grains (Draine & Li 2007). It has been further shown that PAHs can still be excited by the longer-wavelength photons of B stars. Therefore, even though the apparent correlation does not have a physically trivial explanation, it suggests that PAH emission can indeed be used as a tracer of recent star formation.

We do not find any correlation between PAH EWs and the Hα luminosities: SMGs with low EWs may also display luminous Hα emission. This suggests that even for SMGs with a significant AGN mid-IR contribution high SFRs are inferred. We note that the use of Hα as a SFR indicator is vulnerable to uncertainties, even if it has been corrected for extinction using the Hβ/Hα Balmer decrement (Takata et al. 2006). Additional extinction, unaccounted for by the Balmer decrement, may be present and thus remains a caveat. Indeed, as we show in the next section, the degrees of extinction (A_V) estimated for the mid-IR emission in SMGs are significantly higher than measured from the Balmer decrement, as the latter only measures the extinction to regions which are detectable in Hα, with the most extincted regions not contributing at all.

3.5.2 Dust Distribution in SMGs

The range in silicate optical depths we find in SMGs, $\tau_{9.7\mu\mathrm{m}} \sim 0.05$–$1.5$, falls below the typical values reported for both local ULIRGs and AGNs ($< \tau_{9.7\ \mu\mathrm{m}} > \sim 1.5$; Shi et al. 2006; Hao et al. 2007). Recent work by Desai et al. (2007) measured the strength of silicate-absorption features in a large sample of low-redshift ULIRGs from the Bright *IRAS* Sample to find that *cold* ULIRGs, with the steeper mid-IR spectra $S_{25\mu\mathrm{m}}/S_{60\mu\mathrm{m}} \lesssim 0.2$, have deeper silicate-absorption features than *warm* ULIRGs, with $S_{25\mu\mathrm{m}}/S_{60\mu\mathrm{m}} \gtrsim 0.2$. We find that SMGs have $\tau_{9.7\mu\mathrm{m}}$ values close to that of *warm* ULIRGs, such as *IRAS* FSC05189−252, and to the median value found for star-

forming low-redshift galaxies ($<\tau_{9.8\ \mu\mathrm{m}}>= 0.24 \pm 0.10$; see Fig. 3.10). Our observed silicate optical depths correspond to a median visual extinction of $A_V \sim 6$, assuming $A_V = (18 \pm 2) \times \tau_{9.7\ \mu\mathrm{m}}$ (Draine 2003).

The strength of the silicate feature can provide insight into the distribution of dust along the line of sight. The strong silicate absorption measured for *cold* low-redshift ULIRGs can be explained by a small, deeply embedded source with large amounts of obscuring dust along the line of sight (Levenson et al. 2007). Shallower silicate-absorption features and the presence of silicate emission, such as found in both the high-redshift mid-IR-selected sources presented by Sajina et al. (2007) and in *cold* low-redshift ULIRGs suggest that in the mid-IR there is a direct view to the hot thermal continuum source, possibly through a clumpy obscuring medium.

The observed 7.7/6.2 PAH ratios of the SMGs (Fig. 3.9) are also significantly lower than those seen in local nuclear starburst and ULIRG populations. This ratio is potentially sensitive to ionization and reddening, with softer radiation fields and lower obscuration leading to lower 7.7/6.2 ratios. When taken with the differences in silicate absorption, both these results can be explained by a single cause: lower extinction towards the mid-IR line and continuum emitting regions within SMGs, compared to either local nuclear starbursts or ULIRGs. These latter populations are dominated by star-formation activity in highly compact regions and the lower extinction in the SMGs suggests the mid-IR visible star formation in these galaxies is likely to occur in a more extended component, more similar to the activity in the disks of "normal" star-forming galaxies in the local Universe.

Evidence for extended star formation within SMGs has also been found at other wavelengths. High-resolution MERLIN/VLA observations of two samples of SMGs have revealed radio morphologies extending out to $\sim 1''$ or ~ 8 kpc in size (Chapman et al. 2004; Biggs & Ivison 2008). These two studies find that $\sim 85\%$ of the combined sample of 24 SMGs have extended radio emission, while only $\sim 15\%$ appear to be dominated by an unresolved component. Adopting radio emission as a proxy for far-IR emission, these results suggest that massive star formation is occurring on ~ 5 kpc scales within SMGs. This is in contrast to results for local ULIRGs, where the far-IR

emission is confined to a compact nuclear region of $\sim$ 1–2 kpc in size (Charmandaris et al. 2002). Further evidence for physically extended star formation within SMGs has come from studies of their rest-frame optical emission lines. Swinbank et al. (2006) mapped Hα emission from eight SMGs with integral field spectroscopy and found Hα structures extending to 1–2$''$ or $\sim$ 8–16 kpc in size. These results differ, however, from the extent of molecular gas emission in SMGs: sub-arcsecond resolution millimeter imaging of CO emission from six SMGs with the IRAM Plateau de Bure Interferometer suggests compact warm gas distributions in these galaxies, with sizes $\lesssim$ 2 kpc (Tacconi et al. 2006, 2008). These observations typically target the high-J CO transitions, which trace warm and dense gas, so it remains possible that there are more extended reservoirs of cold gas on $\gg$ 2 kpc scales within these systems which could fuel their extended star formation. Our mid-IR results give further evidence towards a more extended distribution of the star-forming regions in SMGs, in contrast to the compact nuclear starbursts seen in similarly luminous local galaxies.

3.6 Conclusions

SMGs are an enigmatic population which have been proposed to undergo a tremendous amount of star-forming activity, in order to explain their ultra-luminous infrared emission. The high stellar masses and SFRs inferred for these galaxies have prompted the idea that SMGs are the likely progenitors of today's most massive galaxies. However, the contribution from AGN activity to the bolometric luminosity has remained a caveat to these results. We present the largest sample of SMGs observed in the mid-IR with *Spitzer* IRS. Our main results are:

1. At the individual level, we find that 80% of SMGs in our sample display strong PAH features, with $L_{7.7\mu\mathrm{m}} \sim 10^{43}$–$10^{45}\,\mathrm{erg\,s^{-1}}$. This confirms for a large sample of SMGs that this is a population undergoing intense star formation, including some of the most intense star-formation events ever witnessed in the Universe.

2. We find only three cases of SMGs with continuum-dominated spectra (12% of our sample), which indicates that even though SMGs appear to be starburst-

dominated as an ensemble, some diversity is present within the sample.

3. We find that SMGs have a spread in optical depths as measured by the strength of the silicate absorption feature at $\lambda \sim 9.7$ μm. However, the mean value is significantly less than local ULIRGs or low-redshift nuclear starburst-dominated galaxies. This difference suggests that SMGs have lower dust obscuration to their mid-IR continuum emitting regions than local ULIRGs.

4. Comparison of PAH flux ratios, $S_{7.7\mu\mathrm{m}}/S_{11.3\mu\mathrm{m}}$, suggests that SMGs host similar radiation environments to local star-forming galaxies. However, the $S_{7.7\mu\mathrm{m}}/S_{6.2\mu\mathrm{m}}$ PAH ratio is lower in SMGs than in local nuclear starbursts or ULIRGs. This can most easily be explained if the extinction to these regions is lower in SMGs than in the local populations.

5. Our composite SMG spectra allow us to make more reliable measurements of the potential AGN contribution as revealed by an enhanced hot-dust continuum at $\lambda_{rest} \sim 10.5$ μm. We make conservative assumptions regarding the AGN contribution and find that the relative contribution of an AGN with respect to star-formation activity remains low. With a maximum AGN contribution of $\lesssim 35\%$ to the total luminous output, SMGs are clearly a galaxy population dominated by intense starburst activity.

6. We conclude that the detailed mid-IR spectra of SMGs show several differences with either local ULIRGs or nuclear starbursts. These differences can be most easily explained by a difference in the extinction to the mid-IR continuum and line emitting regions of these galaxies, with the SMGs showing systematically lower extinction. Given the compact geometry of the mid-IR emission from local ULIRGs, the difference in extinction we see argues that the mid-IR emission in SMGs, both continuum and PAH-emission, arises in a more extended component ($\gg$ 1–2 kpc). This supports radio and Hα studies which indicate that star formation in SMGs is extended on scales of ~ 5 kpc, far larger than seen in local ULIRGs.

Acknowledgements We thank Alexandra Pope, Elisabetta Valiante, Anna Sajina and Bernard Brandl for facilitating results and/or reduced spectra of their *Spitzer*

samples for proper comparison to our galaxies in this work. We are also grateful to Laura Hainline, Patrick Ogle, Vandana Desai and James Geach for helpful discussions.